Analysis of a light permanent magnet in-wheel motor for an electric vehicle with autonomous corner modules

Sergio Romero Pérez

KTH Electrical Engineering

Degree project in
Electrical Engineering
Master of Science
Stockholm, Sweden 2011

XR-EE-EME 2011:001

KTH Electrical Engineering

Analysis of a light permanent magnet in-wheel motor for an electric vehicle with autonomous corner modules

SERGIO ROMERO PÉREZ

Master of Science Thesis in Electrical Machines and Drives
at the School of Electrical Engineering
Royal Institute of Technology
Stockholm, Sweden, February 2011.
Supervisor: Oskar Wallmark
Examiner: Juliette Soulard

XR-EE-EME 2011:001

Analysis of a light permanent magnet in-wheel motor for an electric vehicle with autonomous corner modules
SERGIO ROMERO PÉREZ

School of Electrical Engineering
Department of Electrical Machines and Power Electronics
Kungliga Tekniska Högskolan
SE–100 44 Stockholm
Sweden

Abstract

The use of in-wheel motors is an attractive alternative in small passenger vehicles aimed for transportation in urban areas. The improved control possibilities and the removal of certain components such as the transmission system are some of its advantages. Therefore, this thesis deals with the analysis of an permanent magnet synchronous outer rotor motor aimed for an in-wheel application with the autonomous corner module concept.

First, some basic concepts about permanent magnet motors are reviewed and an analytical model of a permanent magnet outer rotor motor is presented. As a result from this analytical model, three motor configurations are obtained including both distributed and concentrated windings.

Next, finite element method simulations are conducted on the previously obtained motor configurations. Torque-speed curves, voltage-speed curves and losses are computed. Differences with the results obtained using the analytical model are observed due to its simplicity. Both sinusoidal and pulse width modulation currents are used as an input to the motors obtaining considerably different results, especially in terms of losses. Stator skew is introduced for torque ripple reduction and an analytical magnet segmentation model is applied to reduce the magnet losses.

Finally, a thermal analysis is carried out to confirm the thermal viability of the motors under two different driving cycles. The material properties are contrasted with the obtained temperatures to a discard possible magnet demagnetization or insulation failure. It is concluded that the current density in the motors can be increased.

Key words: Finite element analysis, in-wheel motor, permanent-magnet synchronous machine, thermal modeling, thermal transient analysis.

Sammanfattning

Hjulmotorer kan vara ett attraktivt teknikval för små fordon avsedda för transport i urbana miljöer. Fördelarna med denna teknik inkluderar möjligheten att mer exakt kunna reglera de krafter som tas ut från däcken samt det faktum att transmissionssystemet blir betydligt enklare. I detta examensarbete så tas ett flertal hjulmotordesigner av permanentmagnettyp fram avsedda för att passa ett autonomont hjulhörn med givna prestanda.

Först presenteras en övergripande bakgrund om permanentmagnetmotorer och en analytisk modell av en permanentmagnetmotor med yttre rotor presenteras. Som resultat från den analytiska modelleringen erhålls tre motorkonfigurationer där två har en distribuerad lindning och den tredje en koncentrerad lindning.

Sedan har simuleringar med hjälp av finita elementmetoden (FEM) utförts på de erhållna motorkonfigurationerna. Vridmoment och spänning som funktioner av hastighet samt förluster kan därmed beräknas. Ett antal skillnader mellan resultaten från FEM-simuleringarna och den analytiska modellen observerades vilket kan hänvisas till de enkla modeller som den analytiska modellen är uppbygd på. För att beräkna järn- och magnetförluster mer nogrannt så har dessa beräknats både vid antagandet av ideala, sinusformades fasströmmar samt, mer realistiska, fasströmmar erhållna vid pålagd pulsbreddsmodulerad spänning. För att minska kuggmomentet så kan statorn sneddas och sneddningens inverkan på momentkurvformen har därför analyserats. Vidare har en analytisk modell använts för att studera hur magnetförlusterna kan minska vid ökad axiell segmentering.

Slutligen har en termisk analys utförts för att studera hur elmotorerna värms upp vid drift enligt olika körcykler. Speciellt har lindnings- och magnettemperaturer studerats för att undvika isolationsfel samt permanent demagnetisering av magneterna. För de körcykler som studerades framgick från den termiska analysen att det finns utrymme för att öka strömtätheten i ledarna.

Nyckelord: Finita elementmetoden, hjulmotor, permanentmagnetiserad synkronmaskin, termisk modellering, termisk transient analys.

Acknowledgements

This thesis project has received financial support from the Swedish Hybrid Vehicle Centre (SHC), within the “Fault-tolerant over actuated HEVs” research project, which is gratefully acknowledged.

In first place, I would like to sincerely thank Oskar Wallmark for all the help and guidance that he has provided through my work, the important knowledge that he has shared with me and his positive spirit present in every meeting and e-mail.

I am also very grateful to Shafigh Nategh for his help with some of the doubts that arose during the work and to Nima who made my time in the department more comfortable.

Thanks to my friends in Spain, Rober, Marta, Javi, Gil, Pedro, Laura, Clara, Jimy..., to the ones I met in Sweden, Flo, Jörg, Alberto, Zaira, Itzi, Manu, Alfonso... and especially to those who have accompanied me in both countries, Fer and Alvaro, for providing me with so many unforgettable moments. These memories and the moments yet to come give me strength in every step.

Thanks to all my family that has supported and believed in me, especially to my grandma Domi for looking after me so well during my long study periods.

Last, but certainly not least, I would like to thank my parents and my brother for their endless support, advice and love, not only through my time in Sweden, but during all my life. Without them I would not be where I am and none of this would have been possible. I love you very much!

Sergio Romero Pérez
Stockholm, Sweden
February 2011

Contents

Chapter 1

Introduction

This chapter serves as a brief introduction to the background and objectives of this master thesis. Further, in-wheel motors and the autonomous corner module concept are also reviewed.

1.1 Background

The use of light in-wheel motors is an attractive alternative for smaller passenger vehicles aimed mainly for transportation in urban areas. At the Laboratory of Electrical Machines and Power Electronics at the Royal Institute of Technology (KTH), research related to this area is carried out in cooperation with the vehicle dynamics research group also at KTH.

1.2 Objectives

A preliminary in-wheel motor design has already been developed using solely analytical techniques. The aim of this project is to analyze the proposed design using a FEM software package. Important characteristics such as the torque-speed curve, iron losses and torque waveforms have to be obtained. Next, transient thermal simulations using a relevant vehicle drive cycle as input should be computed to reach a final design with a minimized weight and without risking overheating the construction.

The motor has to fulfill a series of specifications which have been considered in the analytical model proposed.

1.3 In-wheel motors

An in-wheel motor, also called wheel hub motor, is an electric motor which is placed inside the wheel hub and drives it directly. The first motor of this kind appeared in 1884

when Wellington Adams patented an electric wheel motor equipped with a complex gear [1].

The design of an in-wheel motor usually consists of an inner stator and an outer rotor which can be fixed to the wheel, making it rotate directly, or coupled by a gearbox. However, inner rotor motors can also be used. By introducing in-wheel motors the transmission system between the motor and the wheels can be eliminated. Differentials, gearboxes and axles are further not needed, suppressing mechanical losses associated with them and, thus, increasing the efficiency of the system. Another positive aspect is that they enable individual control of every wheel, allowing the implementation of several driving functions in a more simple way.

However, the introduction of the motor into the wheel hub brings problems. The electric motor is made out of steel which increases the weight of the wheel. The weight of the wheel is inversely proportional to its ability to follow the profile of the road. Thus, a light wheel will have more grip than a heavy one and transmit less vibrations to the vehicle's cabin, improving the passengers comfort. This effect may be reduced to some extent, since the braking can be mainly done with the wheel motor, reducing the weight of the friction brake.

Recently developed wheel hub motors for automotive use are available with a power-weight ratio of approximately 1 kW/kg (nominal) [8]. However, in-wheel motors are yet not widely applied in the car industry, but several concept cars that incorporate them have recently been presented like the Volvo ReCharge and the Peugeot BB1.

1.4 Autonomous corner modules

Generally, conventional chassis solutions are based on a very hardware oriented design philosophy. This means that new product evolutions need a considerable redesign effort even if the intended change is small. To meet the demand of a more software oriented product development, in which the functions are implemented by software instead of a thorough chassis redesign, the autonomous corner module (ACM) was invented at Volvo Car Corporation (VCC) in 1998 [21].

The ACM concept is based on an individual actuation and control of each wheel's steering, camber, suspension and torque. The control of all these variables independently in every wheel makes the vehicle an over-actuated system in which the number of states intended to be controlled is smaller than the number of actuators. This broadens the control possibilities of the vehicle, permitting improvements in safety or efficiency, but also introduces a complexity that has to be technically solved [8].

The ACM design consists of a wheel hub, equipped with an in-wheel motor, which is actively controlled from three points: one in the upper and two in the lower part of the hub. The upper point is connected to an actuator that controls the vertical load of the vehicle and is in charge of the suspension, independently of the vehicle's static mass

which is damped by a conventional spring. The lower points are connected to actuators that control the steering as well as the wheel camber. An extra arm joins the two lower actuators to avoid side forces on them.

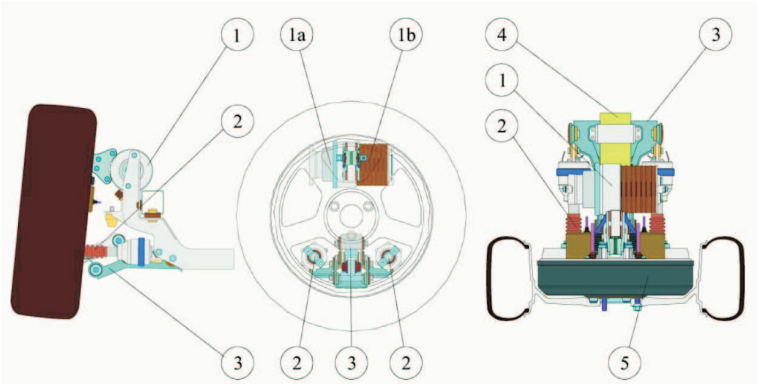

Fig. 1.1 ACM design proposal showing front, side and top views. 1) Damper a) with adjustable spring b), 2) Steer actuators, 3) Lower arm, 4) Leaf spring, 5) In wheel motor [8].

Chapter 2

Analytical model of a PM synchronous machine

In this chapter, an analytical model of a permanent magnet synchronous machine is reviewed. Both, distributed and concentrated winding configurations are considered. Finally, three resulting motor models are presented and compared.

2.1 Permanent magnets

Permanent magnets (PMs), also called hard magnetic materials, are materials that are permanently magnetized and produce a magnetic field. In motor technology, this property can be used to produce a magnetic field in the air gap without the use of an excitation winding.

PMs can be described by their B-H hysteresis loop. The most important part of this curve is called the demagnetization curve and is located in the second quadrant (see Fig. 2.1). When a PM is exposed to a reverse magnetic field intensity, its magnetic flux density drops. In modern magnetic materials, the B-H curve is almost linear down to a point were it drops sharply. If a reverse magnetic field intensity does not make the PM abandon this linear part, the magnet will recover its remanent magnetization B_r when the field disappears. However, if the reverse magnetic field intensity applied is strong enough to make the magnetic flux density trespass the point where the curve bends, the magnet will enter the irreversible demagnetization zone. If this happens, the magnet will follow another recoil line when the magnetic field disappears and recover a remanent magnetization value under the original, i.e., the magnet will demagnetize. The main parameters that characterize a PM are [3]:

- **Saturation magnetic flux density** B_{sat} and its corresponding H_{sat}. At this point of operation, the alignment of all the magnetic moment of domains is in the direction of the external magnetic field applied.

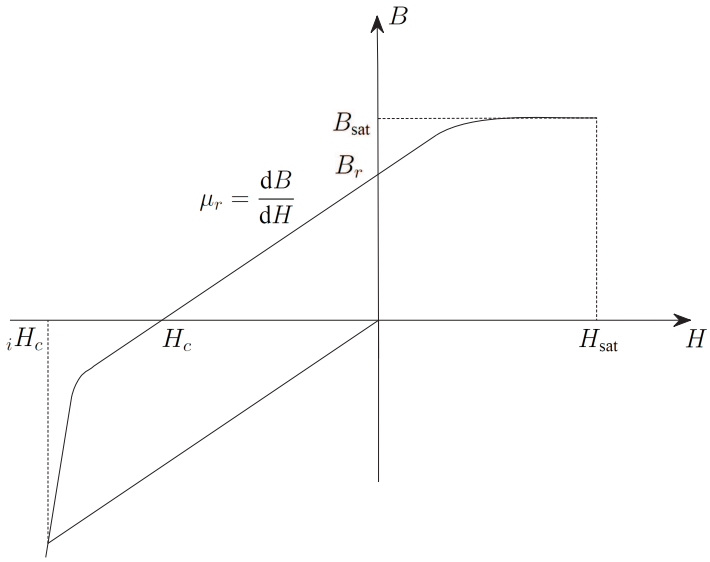

Fig. 2.1 Demagnetization curve of a PM.

- **Remanence** B_r is the magnetic flux density at zero magnetic field density.
- **Coercivity** H_c is the value of the demagnetization field intensity needed to bring the magnetic flux density to zero. The higher the coercivity, the thinner are the magnets required to withstand the demagnetizing field.
- **Intrinsic coercivity** ${}_iH_c$ is the value of the demagnetization field intensity needed to permanently demagnetize the material.
- **Magnetic permeability** μ_r is the steepness of the demagnetization curve.

2.2 PM synchronous machines

The use of permanent magnets in the construction of synchronous machines has some advantages with respect to electromagnetic excitation [3]:

- No electrical energy is absorbed by the excitation system. Thus, there are no excitation losses which enable a subsequent increase in efficiency.
- Higher torque and/or output power per volume.
- Better dynamic performance (higher magnetic flux density in the air gap).
- Simplification of construction and maintenance.

However, there also disadvantages associated with this type of machines:

- The high price of the PM material.

- The fact that the magnets are temperature sensitive and become permanently demagnetized above a certain threshold temperature.

- The fact that a position sensor or a rotor angle estimation method is required for converter-fed applications.

There are three different PMSM topologies according to the direction of magnetization: radial-flux, axial-flux and transverse-flux machines. Only the radial-flux type is considered in this report. There are also several configurations within this topology according to the magnet placement and if the rotor is mounted inside or outside the stator.

2.2.1 Magnet placement

According to the placement of the magnets, the radial-flux PMSM can be divided in three categories: surface mounted PM machines, inset PM machines and buried or interior PM machines.

Surface mounted PM machines have the magnets glued to the rotor surface. The main advantage of this configurations is its simplicity and, consequently, its low price. However, the magnets are, in this case, exposed to demagnetization fields. The magnets of inset PM machines are glued into slots made in the rotor. Therefore, these machines are also simple and have a reluctance torque due to their saliency. The last type, buried PM machines, have the magnets placed inside the rotor steel. However, there are several possibilities to do this, such as v-shaped or tangentially magnetized PM machines. The main advantages of this configuration are a concentrated flux in the rotor which makes it possible to achieve a high open-circuit flux density, the associated saliency which produces reluctance torque and the improved protection against demagnetization [13].

2.2.2 Rotor topology

According to the rotor configuration there are two possibilities: inner and outer rotor. The outer rotor solution is well adapted to in-wheel motors since the rotor can be directly fixed to the wheel. It is also easier to wind the stator since the stator teeth point outwards. Moreover, outer rotor designs are around 15% lighter than an inner rotor machine with the same torque because of their longer air gap diameter. Since the torque of the machine depends on this value squared, the axial length can be reduced with the subsequent weight reduction [13]. However, outer rotor machines may be more difficult to refrigerate in some applications since the windings, which normally generate the highest losses, are placed in the inner part of the machine [4].

2.2.3 Winding configurations

For a three phase machine, the number of slots per pole and phase q is given by

$$q = \frac{Q}{3p} \tag{2.1}$$

where Q is the total number of slots and p is the number of poles. If this value is an integer, the winding is referred to as a distributed winding. The higher the value of q, the more sinusoidal the MMF-wave produced by the windings will be [15]. Distributed winding machines machines can be single-layered with one coil side per slot or double-layered where the coil goes from the bottom of one slot to the top of another.

If each coil is wound around one tooth, the winding is referred to as a concentrated winding (here q is not an integer). PMSMs with concentrated windings are, in some applications, a competitive alternative to distributed windings. With them, it is possible to achieve a low cogging torque, a long constant power speed range and a good fault tolerance [13]. The resulting end windings of concentrated windings are also shorter than the ones of a distributed winding machine.

Concentrated windings can be single-layered, with alternate wound teeth, i.e., one coil side per slot, or double-layered, with all the tooth wounded and two coils sharing one slot. Double-layered concentrated windings produce less losses and torque ripple whereas single-layered concentrated windings provide a high fault tolerance since the different phases are isolated [13].

2.2.4 Fundamental relations

Speed

In the steady state, the mechanical speed of the machine in rpm is given by

$$n = \frac{60 \cdot f}{p/2} \tag{2.2}$$

where f is the input frequency and p the number of poles.

Torque

The torque equation for a general inner rotor topology can be expressed as

$$T_e = \frac{4}{\pi} \hat{S}_1 \hat{B}_\delta f_{w1} \left(D - \delta\right)^2 L \sin\beta \tag{2.3}$$

where $\hat{S}_1$ is the peak fundamental current loading, $\hat{B}_\delta$ is the peak fundamental open-circuit air gap flux density, f_{w1} is the fundamental winding factor, D is the inner stator diameter, δ is the air gap length, L the active length and β the angle between the d-axis and the current vector [13].

Eq. (2.3) points out the influence of some of the design parameters in the torque of the machine. If the torque is fixed, the current loading $\hat{S}_1$ is directly related to the slot area which size influences the dimension of the air gap diameter $(D-\delta)$. The air gap diameter is also limited by the external diameter. The fundamental winding factor f_{w1} varies with the winding configuration and a lower value should be compensated with a higher current loading, open circuit air gap flux density or active length. B_δ is limited by the magnet weight and price and the active length influences the magnet weight and the total weight of the machine. Finally, the angle β is determined by the saliency of the machine [13].

2.2.5 Losses

Copper losses

The losses in the machine windings are pure resistive and can be expressed as

$$P_{\text{Cu}} = 3R_s i^2 \tag{2.4}$$

where R_s is the stator resistance and i is the rms phase current.

Iron losses

The iron losses consist of hysteresis and Joule losses. Hysteresis losses arise due to the magnetic properties of the steel. The magnetic particles of the steel tend to line up with the magnetic field. However, the magnetic field changes its position while the machine is rotating, and the particles have to be continuously moving to align themselves. This particle movement causes friction between them and, thus, produces heat. Assuming a purely sinusoidal flux density variation, the hysteresis losses per mass unit can be expressed as

$$P_{\text{hyst}} = k_{\text{hyst}} \omega B^\beta \tag{2.5}$$

where k_{hyst} is the hysteresis constant for the steel, ω is the electrical angular speed, B is the peak magnetic flux density and β is the Steinmetz constant which is a property of the steel [15].

Joule losses are caused by the induced currents in the steel. As the magnetic flux is varying, eddy currents are induced in the steel which produce resistive losses. Eddy current losses per mass unit follow

$$P_{\text{eddy}} = k_{\text{eddy}} \omega^2 B^2 \tag{2.6}$$

where k_{eddy} is the eddy current constant for the steel [15].

2.3 Motor topology selection

The motors for further study are chosen to be surface-mounted PM synchronous motors with an outer rotor. Some advantages of this configuration are:

- A higher number of poles is allowed due to the larger rotor diameter compared to inner rotor motors [10].
- The magnets are exerted against the rotor during the rotational movement which makes their detachment more difficult [10].
- The structure is well adapted to in-wheel motors since the wheel can be directly coupled to the outer rotor.

2.4 Surface mounted PM motors with an outer rotor

A PMSM with an outer rotor consists of an inner wounded stator and an outer rotor with permanent magnets. These magnets supply the magnetic field that interacts with the stator currents to create the necessary torque.

2.4.1 Geometry

The motor geometry and its parameters are represented in Fig. 2.2. The relations between the different geometrical parameters are found as

$$r_\delta = r_{out} - h_{ry} - h_m - \delta \tag{2.7}$$

$$b_{ss1} = \frac{2\pi\left(r_\delta - h_{sw}\right)}{3pq} - b_{st} \tag{2.8}$$

$$b_{ss2} = \frac{2\pi\left(r_\delta - h_{ss}\right)}{3pq} - b_{st} \tag{2.9}$$

$$h_{sy} = r_\delta - h_{ss} - r_{in} \tag{2.10}$$

$$\alpha = \frac{\alpha_{\text{elec}}}{p/2} \tag{2.11}$$

where p is the number of poles, q is the number of slots per pole and phase and α_{elec} represents the electrical angle covered by the magnets. The width of a stator tooth b_{st} is constant along the whole tooth section. For the geometrical calculations, b_{ss1}, b_{ss2} and b_{st} are approximated as straight lines instead of arcs of circumference.

2.4.2 Current and torque dynamics

The equations that describe the motor behavior are presented in this section. The peak fundamental phase voltage E of a PM motor is produced by the magnets according to the expression,

$$E = \omega\psi_m \tag{2.12}$$

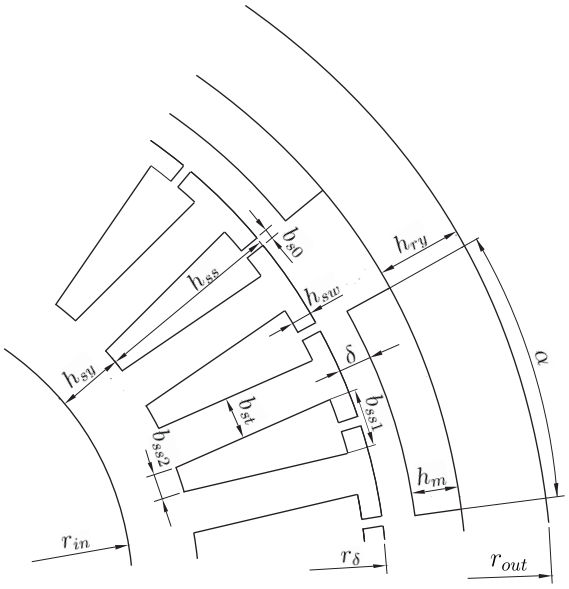

Fig. 2.2 Geometrical parameters.

where ψ_m is the permanent-magnet flux linkage and ω is the electrical synchronous angular speed. In the steady state and if neglecting harmonics, the voltage d- and q- components of the motor can be expressed as

$$u_d = R_s i_d - \omega \psi_q = R_s i_d - \omega L_q i_q \tag{2.13}$$

$$u_q = R_s i_q + \omega \psi_d = R_s i_q + \omega \left(\psi_m + L_d i_d \right). \tag{2.14}$$

The torque is given by (2.15) (a complete deduction of it can be found in, e.g., [15]).

$$T_e = \frac{3}{2}\frac{p}{2}\left[\psi_m i_q - \left(L_q - L_d \right) i_q i_d \right] \tag{2.15}$$

In this case, since the magnets are surface mounted, the air paths in d- and q-directions have the same length which means that $L_d = L_q = L_s$. Thus, the torque expression can be simplified to

$$T_e = \frac{3}{4} p \psi_m i_q. \tag{2.16}$$

2.4.3 Motor parameters and relations

Some important relations for the motor design are presented in this section. The fundamental winding factor for a distributed winding motor with q slots per pole and phase is given by

$$f_{w1} = \frac{1}{q} \frac{\sin\left(\frac{\pi}{6}\right)}{\sin\left(\frac{\pi}{6q}\right)} \sin\left(\frac{y_{sp}\pi}{6q}\right) \tag{2.17}$$

where y_{sp} is the pitch length measured in number of slots [15].

Neglecting magnetic saturation, the expression for the synchronous inductance L_s of a surface mounted inner rotor permanent magnet motor is reported in [15] and it can be rewritten for an outer rotor motor as

$$L_s = \frac{3}{\pi} \frac{2\mu_0 \left(r_{\text{out}} - h_{ry} - h_m - c_f\delta\right) L}{c_f\delta + h_m/\mu_r} (f_{w1} q n_s)^2 \tag{2.18}$$

where μ_o and μ_r are the relative permeability of the vacuum and magnets respectively, r_{out} is the outer radius of the motor, h_{ry} is the rotor yoke height, h_m is the magnet height, δ is the air gap length, L is the active length of the motor, f_{w1} is the fundamental winding factor, n_s is the number of turns per slot and c_f is the Carter factor which accounts for the equivalent air gap including the effect of the stator slots.

2.4.4 Current operating points

The motor torque capability is limited by the maximum current and by the dc-link voltage supplied by the battery. These limitations can be summarized as

$$\sqrt{i_d^2 + i_q^2} \leq i_{\text{max}} \tag{2.19}$$

$$\sqrt{u_d^2 + u_q^2} \leq u_{\text{max}} = \frac{u_{\text{dc}}}{\sqrt{3}}. \tag{2.20}$$

If the resistive voltage drop is neglected, (2.13) and (2.14) can be rewritten as

$$u_d = -\omega L_s i_q \tag{2.21}$$

$$u_q = \omega \left(\psi_m + L_s i_d\right). \tag{2.22}$$

By substituting (2.21) and (2.22) in (2.20), the following relation is obtained

$$\left(i_d + \frac{\psi_m}{L_s}\right)^2 + i_q^2 \leq \left(\frac{u_{\text{max}}}{\omega L_s}\right)^2 \tag{2.23}$$

which in the dq-current plane describes a circle of radius $u_{\text{max}}/\omega L_s$ and centered in ($-\psi_m/L_s$,0) in which the voltage restriction is fulfilled. Together with the maximum current restriction (2.19), this describes the possible operation points of the motor for all speeds. Such a map is presented in Fig. 2.3.

As seen in (2.16), the motor torque depends only on the q-axis current component. Thus, in order to minimize the resistive losses, $i_d = 0$ and $i_q \neq 0$ should be selected. In Fig. 2.3, the red line represents the trajectory followed to obtain the maximum torque at different speeds. The maximum torque point is the intersection between the voltage and current restrictions. The green lines represent the trajectories followed to achieve different torque values at a constant speed.

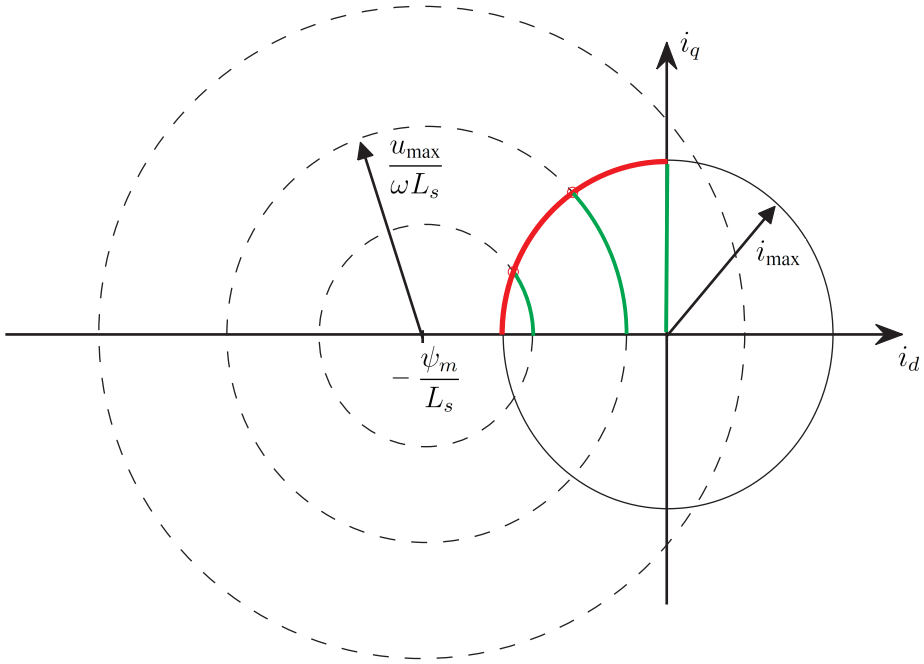

Fig. 2.3 Operating points with the flux weakening technique.

2.4.5 Losses

Copper losses

In the analytical model, the fundamental copper losses can be expressed as

$$P = \frac{3}{2} R_s \left(i_d^2 + i_q^2 \right) \tag{2.24}$$

where R_s is the stator phase resistance and the factor $\left(i_d^2 + i_q^2 \right)$ is the peak fundamental phase current squared.

Iron losses

To account for the motor iron losses, both hysteresis and eddy current losses are considered. The losses are calculated separately in the stator yoke and teeth with (2.25) and (2.26), respectively:

$$P_{sy} = \left(k_{\text{hyst}} \omega B_{sy}^{\beta} + k_{\text{eddy}} \omega^2 B_{sy}^2 \right) m_{sy} \tag{2.25}$$

where m_{sy} is the stator yoke weight.

$$P_{st} = \left(k_{\text{hyst}} \omega B_{st}^{\beta} + 12q \frac{b_{ss} + b_{st}}{\pi^2 b_{st}} k_{\text{eddy}} \omega^2 B_{sy}^2 \right) m_{st} \tag{2.26}$$

where m_{st} is the stator teeth weight.

2.5 Design of a PMSM with distributed windings

The design of the motor turns out to be an optimization problem which will give the best possible configuration according to some criteria.

2.5.1 Objective function

There are different possible criteria when designing a specific motor. At first sight, the motor efficiency appears to be an attractive choice not only from the environmental point of view, but also when considering the electric vehicle's autonomy. However, since the motor will be mounted inside the wheels of an electric car, the priority is to minimize its weight. The reason for this is the problem that may arise with the unsprung mass as described in Chapter 1. Besides, a light motor requires less material which may also be positive from an economical point of view. Thus, the design objective function chosen is the active weight of the motor which has to be minimized. This includes the weight of the steel, windings and magnets.

2.5.2 Design variables

The design variables are six: the number of poles, the number of slots per pole and phase, the number of turns per slot, maximal peak phase current, rotor back thickness and active length. These are the parameters varied in the optimization problem to find the motor configuration. The variables and its range are presented in Table 2.1.

Table 2.1: Design variables.

Variable	Symbol	Range
Number of poles	p	$2 \leq p \leq 30$, p is even
Slots per pole and phase	q	$1 \leq q \leq 3$
Number of turns per slot	n_s	$1 \leq n_s \leq 100$
Maximal peak phase current	i_{max}	0 A $< i_{\text{max}} <$ 100 A
Rotor back thickness	h_{ry}	$h_{ry} \geq 9$ mm
Active length	L	$L \geq 30$ mm

2.5.3 Constants

The values presented in Table 2.2 are derived from the material properties and some typical design data. They are considered as constants for the analytical design of the motor.

Table 2.2: Constants.

	Constant	Symbol	Value
Magnet	Remanent flux density	B_r	1.2 T
	Relative permeability	μ_r	1.05
	Magnet density	ρ_m	7700 kg/m^3
Iron	Steel density	ρ_s	7700 kg/m^3
	Eddy loss constant	k_{eddy}	1.1903·10^{-6}
	Hysteresis loss constant	k_{hyst}	0.0031
	Steinmetz constant	β	2
Winding	Copper density	ρ_{Cu}	8930 kg/m^3
	Copper resistivity	r_{Cu}	2.392·10^{-8}
	Copper fill factor	ff	0.45
	Slot insulation thickness		0.2 mm
	Slot wedge thickness		2 mm

2.5.4 Requirements

According to the future motor function, there are some requirements that the motor design must fulfill. They are basically related to the specifications that are required to operate the vehicle, the physical constraints of the motor placement and the feeding limitations of the battery that will supply the power. These requirements are presented in Table 2.3.

Table 2.3: Requirements.

Rated torque	T_r	170 Nm
Rated speed	n_r	850 rpm
Torque at maximum speed	$T_{n,\text{max}}$	40 Nm
Maximum speed	n_{max}	1872 rpm
Minimum inner radius	$r_{\text{in,min}}$	148 mm
Outer radius	r_{out}	216 mm
Minimum dc-voltage	$u_{\text{dc,min}}$	400 V

2.5.5 Fixed values and constraints

In the design process, some values are chosen to be fixed and there are also some restrictions that must be fulfilled. They are presented in Table 2.4.

The air gap length δ is normally in the range of 1–3 mm in a PM-motor [15]. The longer the air gap length, the more magnetic material is needed to achieve the required air-gap flux density and the smaller the synchronous inductance.

Table 2.4: Fixed values and constraints.

Peak fund. flux density in stator yoke	B_{sy}	1.6 T
Peak fund. flux density in teeth	B_{st}	1.6 T
Peak fund. flux density in rotor yoke	$B_{ry,\text{max}}$	1.6 T
Max. peak fund. current density	J_{max}	$\sqrt{2}\cdot 10^6$ A/m^2
Max. peak fund. current loading	$S_{1,\text{max}}$	$80\cdot 10^3$ A/m
Air gap length	δ	1 mm
Electrical magnet angle	α_{elec}	120°
Magnet height	h_m	2.5 mm $\leq h_m \leq$ 10 mm

2.5.6 Design procedure

With the variables, constants and parameters described in the previous sections, the design procedure follows a scheme showed in Fig. 2.4. The process starts varying the design variables, then the different motor parameters and values are computed to determine the viability of the configuration and finally determine the value of the objective function. The different possible motor configurations are stored to finally select the one that optimizes the design. As mentioned before, the motor weight was the objective function which determined the best solution in this case.

2.6 Design of a PMSM with concentrated windings

The design procedure for the PMSM with concentrated windings is very similar to the one with distributed windings. The objective function, constants, requirements, fixed values and constraints are kept the same. Also the design procedure is identical to the one with distributed windings. There are just a few aspects that have to be taken into account.

- Instead of the slots per pole and phase q, the total number of slots Q is used as design variable. This is made because in this kind of motors, the first parameter is not an integer, making it difficult to set as a design variable.

- The copper fill factor is increased to $ff = 0.6$. This is because in concentrated winding motors the stator can be built in segments which enables a higher degree of automation with a better control of the coils during the production process. Thus, the winding efficiency is higher [12].

- The winding factor can no longer be calculated as in the motor with distributed windings. The following section will review how it was determined.

2.6.1 Winding factor

In a concentrated winding motor, the pole/slot combination chosen is a key parameter. How to calculate the winding factor for this winding configuration is explained in [13]. Complete tables with the different winding factors values for different combinations of pole numbers and slot numbers are also reported in [13] or [11].

A high winding factor does not always result in good motor properties. When all the coil sides of a phase are placed in the same motor side, unwanted unbalanced magnetic pull is produced [9]. The pole/slot combinations giving winding layouts without any symmetry such as combinations with $Q = 9 + 6k, k = 0, 1, 2...$ and $p = Q \pm 1$ are therefore not recommended [11]. Thus, those combinations were not taken into account in the analytical design of the motor.

2.7 Results and model comparison

Running the previously described simulations, different motor models are obtained. From these models, three are chosen to carry out a more detailed analysis with FEM simulations. They are presented briefly in Table 2.5. The full motor specifications are appended in Appendix A.

Table 2.5: Solutions.

	Motor 1	Motor 2	Motor 3
Winding type	DW	DW	CW
Pole number	16	26	28
Slot number	96	78	30
Turns per slot	11	10	27
Max. peak current (A)	59.4	75.0	77.0
Rotor back thickness (mm)	16	10	9
Active length (mm)	30	30	30
Active weight (kg)	17.0	12.2	12.6

Both, distributed and concentrated winding configurations may be suitable and, therefore, Motor 2 and Motor 3 were chosen. However, despite the lightest configuration with distributed windings is Motor 2, the pole number may be too high creating inadmissible iron losses. Thus, a second motor with distributed windings, but a lower number of poles is chosen in Motor 1. Only one model is taken from the concentrated windings type: Motor 3.

The torque-speed and voltage-speed analytical curves of the three configurations are shown in Fig. 2.5. It shows that Motor 2 and Motor 3 are not only lighter than Motor 1 but can also achieve higher torque at high speed. The predicted motor losses are reported

in Table 2.6. The efficiencies of the three motors are similar, being Motor 2 the one that has the highest value due to its lower copper losses.

Table 2.6: Losses and efficiency.

	Copper	Iron	Efficiency
Motor 1	1.09 kW	0.07 kW	0.93
Motor 2	0.76 kW	0.09 kW	0.95
Motor 3	1.21 kW	0.07 kW	0.92

All the results obtained in this analysis are based on simple analytical models only. Moreover, some simplifications have been made and thus, a further FEM study is carried out in Chapter 3 to verify their validity.

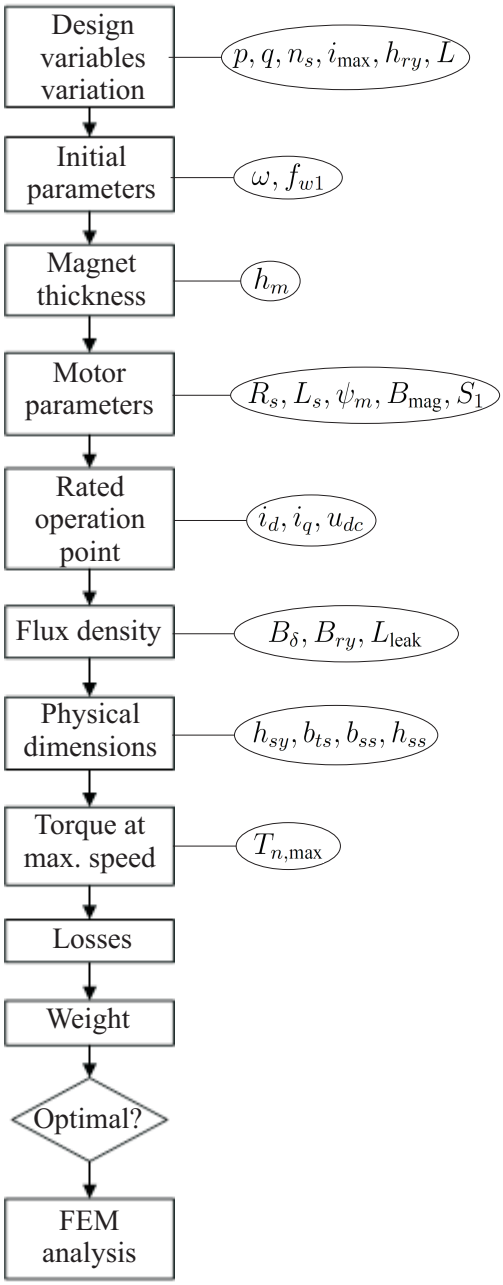

Fig. 2.4 Analytical design flow.

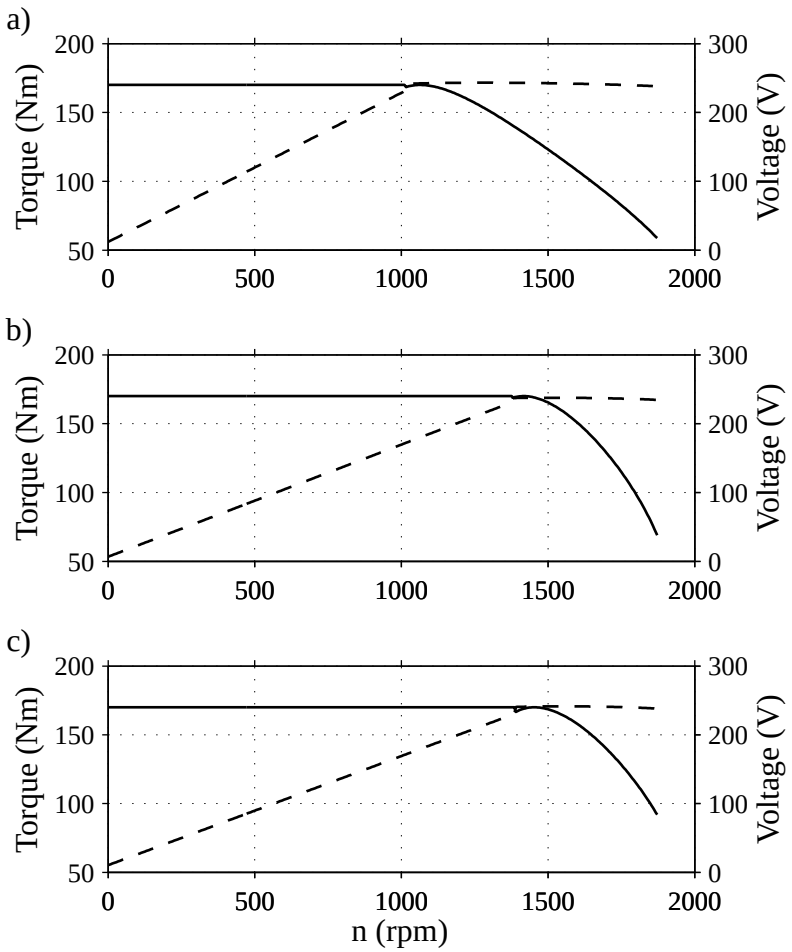

Fig. 2.5 Torque-speed (solid line) and required voltage (dashed line) curves for the motors in consideration: a) Motor 1; b) Motor 2; c) Motor 3.

Chapter 3

Finite element analysis

In this chapter, an analysis using the finite element method (FEM) of the three motors obtained in the previous chapter is carried out. Basic setting of the analysis are described and the solutions are presented. A method to reduce the torque ripple and the magnet losses is also reviewed and applied. Both, analysis using sinusoidal currents and pulse width modulation (PWM) currents are conducted and compared.

3.1 Initial considerations

The FEM software used in this thesis is JMAG-Designer[1]. For the analysis presented in this thesis, only 2D simulations are carried out. Due to the short active length (30 mm) of the motors studied, the end effects are likely not insignificant. Therefore, it would be interesting to accomplish a 3D study to take in consideration the end effects and see how the results differ from the ones approximated with the 2D study presented here.

3.2 Materials

The materials used to model the motors are presented in this section. In this FEM analysis, temperatures are not taken into account and all the material properties are, hence, modeled as temperature invariant.

3.2.1 Electrical steel

The stator and the rotor of the motor are made of laminated steel. The thinner the steel laminations used, the lower the iron losses will become, but on the other hand, the price of the motor will rise. The lamination factor is considered to be 96% and, thus, set in the simulations.

[1] JMAG-Designer is a registered trademark of the Japan Research Institute, Limited.

The selected steel is M235-35A (0.35 mm) and is provided by Surahammars Bruk AB. The B-H curve of the material is presented in Fig. 3.1 and the magnetic loss curves in Fig. 3.2. Table 3.1 contains other important properties of the material.

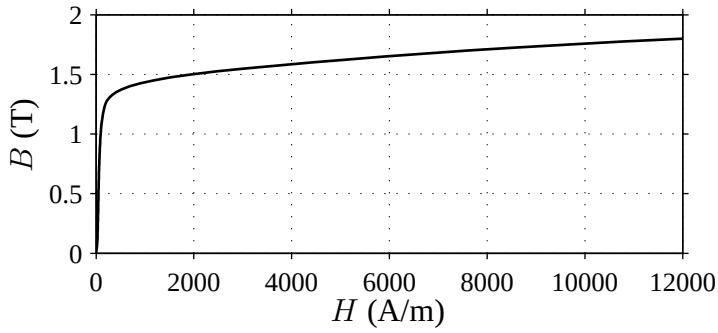

Fig. 3.1 M235-35A steel B-H curve at 50 Hz.

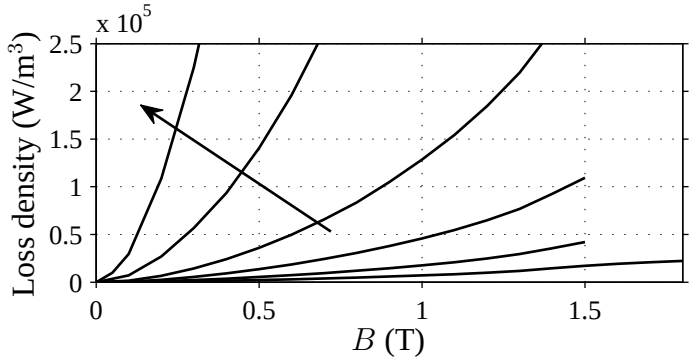

Fig. 3.2 M235-35A steel magnetic loss curves at 50 Hz, 100 Hz, 200 Hz, 400 Hz, 1000 Hz and 2500 Hz. The arrow denotes the direction of increasing frequency.

Table 3.1: Steel properties.

Density	7600 kg/m^3
Electric resistivity	590 nΩm

3.2.2 Permanent magnets

The magnetic material selected is Vacodym 854[2] provided by Vacuumschmelze GmbH & Co. The demagnetization curves at different temperatures are shown in Fig. 3.3. However, for the FEM analysis, the material was modeled using its coercive force and relative

[2]Vacodym is a registered trademark of Vacuumschmelze GmbH & Co.

permeability. The properties correspond to ambient temperature and are displayed in Table 3.2.

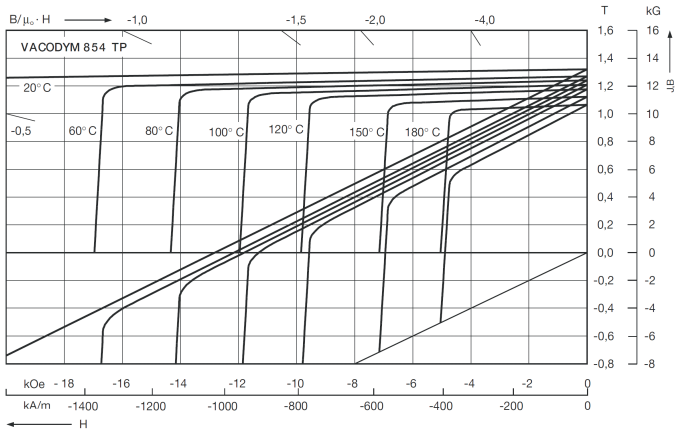

Fig. 3.3 Typical demagnetization curves $B(H)$ for Vacodym 854 TP at different temperatures [19].

Table 3.2: VACODYM 854 properties.

Coercive force	1031000 A/m
Relative permeability	1.05
Density	7700 kg/m^3
Electric resistivity	1.5 $\mu\Omega$m

The operating points of the magnet will have to be checked after the thermal analysis. It is necessary that the magnets never operate in the irreversible demagnetization zone in order to avoid permanent demagnetization. This would irreversibly change their properties and, thus, the complete behavior of the motors.

3.3 Motor models

The motor models used have the exact dimensions of the resulting models of the analytical study and, thus, some simplifications are still considered. The tooth tip angle is set to zero degrees and the slot corner radius is also neglected. This keeps the tooth and slot geometry in a primitive shape that should be reviewed in a more detailed study. Teeth shape optimization in concentrated winding permanent-magnet motors is discussed in [20]. For Motor 1 and Motor 2, only one pole of the motor will be analyzed, taking advantage of the symmetry of the motor. This will save time in the simulations. However, for the concentrated windings motor (Motor 3), this is not possible and the whole motor has to be simulated with the consequent time increase in all the calculations.

3.4 FEM analysis settings

The most important setting made in the FEM analysis will be described in this section.

3.4.1 Conditions

The initial rotor position has to be set in order to match the direction of the magnetic field created by the stator currents in that moment. Thus, an initial rotor angle is introduced for each motor. To account for eddy currents in the magnets, which are typically a 3D issue, in a 2D study, the total eddy currents in each magnet have to be set to zero by introducing a FEM conductor in them and connecting it to ground. This will assure that the amount of upward and downward magnet currents is the same and, thus, the approximate eddy currents are considered.

3.4.2 Simulation time

In all three FEM models, the motors are simulated during one electrical period. For the simulations with sinusoidal currents, this electrical period is divided into 200 steps. Thus, for every speed the simulation time is different but the number of steps that divide the period is kept constant. For the simulations with PWM currents, the number of steps per period is increased to 500 in order to consider the current's high frequency ripple introduced.

3.4.3 Computational mesh

The mesh has to be small enough to avoid having big numerical errors. For Motor 1 and Motor 2 the element size is set to 1 mm. Due to simulating time constraints, a 3 mm element size is chosen for Motor 3. However, an adaptive mesh is set in all three models which subdivides those elements which largely affect the results into smaller ones. In this way, the stator teeth's outer borders are automatically reset to a smaller element size. Fig. 3.4 shows the mesh set for the simulation of Motor 1. To account for magnet losses with good accuracy, the element size is set to 0.5 mm in the magnets of Motor 1 and Motor 2 and to 1 mm in the magnets of Motor 3.

3.5 FEM simulation with sinusoidal currents

In first place, the three motor solutions are simulated using sinusoidal currents as input. This will give an overview on how the motors would behave under ideal feeding conditions.

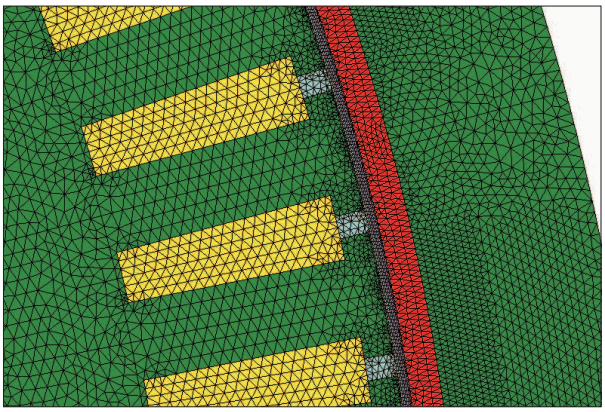

Fig. 3.4 Mesh of Motor 1.

3.5.1 Torque speed curves

The results from the FEM simulations are presented and compared with the analytical results in Fig. 3.5. The dc-link voltage considered in the FEM simulations is 350 V which is a more conservative value than the one considered in the analytical case (400 V). The consequence of this is that the flux weakening technique is applied earlier in the case of the FEM simulations. However, it can be seen from the results that the torque capability of the motors at high speeds is better than what was predicted with the analytical model in all three cases. If the dc-link voltage would have been kept at 400 V, the constant part of the torque curves would have been longer and the voltage would have increased linearly up to that value.

The differences between the analytical and the FEM results are reasonable since the analytical model is fairly simple and, therefore, some simplifications have been introduced such as constant inductances.

Torque ripple reduction

The torque of the motor is not perfectly constant but varying with the rotor position. This torque ripple is caused by the different magnetic circuit permeances that the magnets sense due to the stator slots. This is also known as cogging torque and can also be seen in absence of currents. Also magnetic saturation causes a permeance variation. If saturation is neglected and the number of phases is 3, cogging creates a pulsation with a frequency of

$$f_{\text{cog}} = 6qf \tag{3.1}$$

where q is the number of slots per pole and phase and f is the supply frequency [15]. The cogging frequency can also be expressed in terms of the rotational speed as

$$f_{\text{cog}} = 3qp\frac{n}{60} \tag{3.2}$$

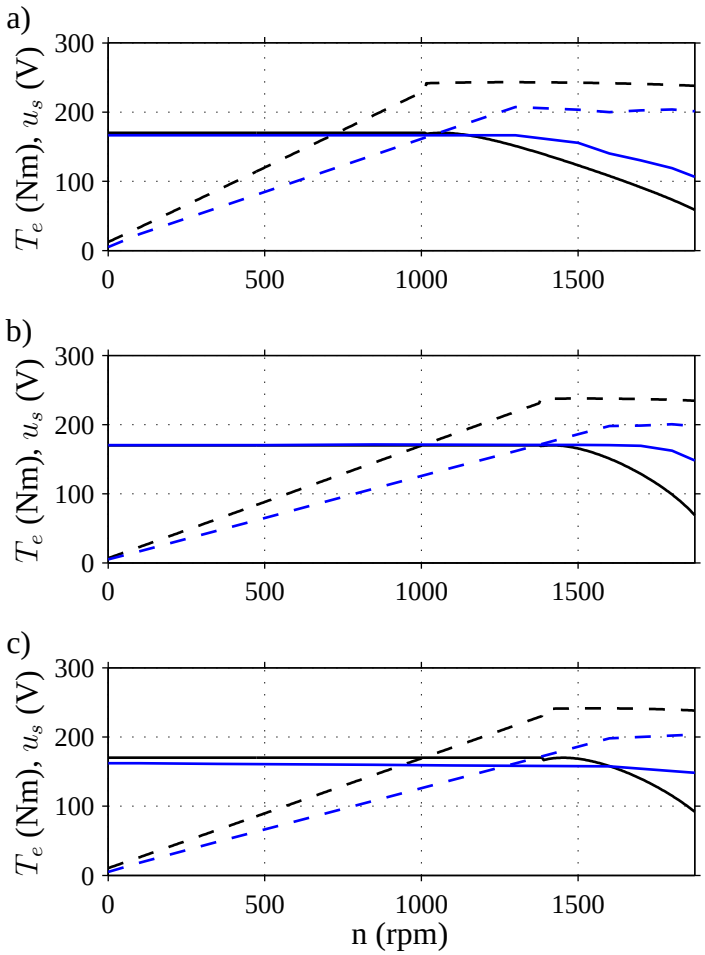

Fig. 3.5 Torque-speed (solid line) and required voltage (dashed line) curves for the motors in consideration: a) Motor 1; b) Motor 2; c) Motor 3. The black and blue lines correspond to the analytical and FEM results respectively.

being p the number of poles and n the rotational speed in rpm.

The cogging torque of Motor 2 is shown in Fig. 3.6. It can be seen that the frequency of the pulsations is six times the value of the supply frequency which corresponds to the frequency given by (3.1).

Other sources of torque ripple include [13]:

- The interaction between the spacial harmonics in the magnetic field produced by the magnets and the windings.
- The interaction between the time harmonics in the magnetic field produced by the inverter and the rotor field.
- Imperfections such as rotor eccentricity or uneven magnet magnetization.

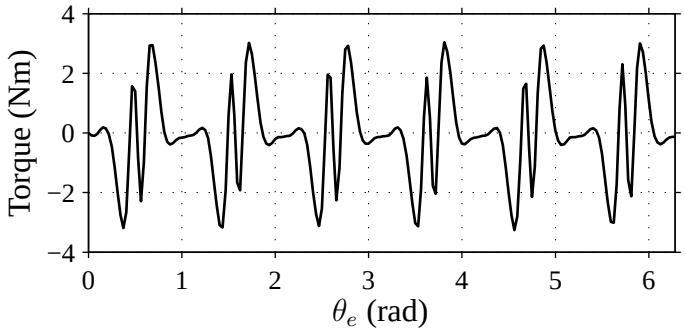

Fig. 3.6 Cogging torque of Motor 2 at open circuit and rated speed.

It is important to reduce the torque ripple, especially in low speed drives, in order to reduce the motor noise and vibration. In a PMSM, this effect also creates difficulties for the control systems to determine the speed and position. There are different possibilities to reduce the torque ripple of the motor:

- Skewing the stator or the rotor magnets.
- Control based techniques in which the current shape forces an additional torque that cancels the pulsation [7].
- Give and appropriate shape to the magnets in order to produce a more sinusoidal flux density in the air gap [15].

However, the resulting torque ripple from PMSMs with concentrated windings is normally low. Thus, a correct choice in the pole slot combination may be enough to achieve an acceptable ripple. If the least common multiple of the pole number and slot number is large, a low cogging torque can be achieved [13].

In this thesis, skewing the stator is the option considered to reduce the cogging torque. This is made by adding the contribution of the different stator sheets displaced a certain angle. The torque of a motor with a skewed stator can be computed from the resulting torque of a non skewed stator as

$$T(\theta) = \frac{1}{L}\int_0^{\theta_s} T\left(\theta + z\frac{\theta_s}{L}\right) dz \tag{3.3}$$

where L is the active length of the motor and θ_s is the skew angle.

The skew chosen is 1 slot for the distributed winding motors and 1/3 slots for the concentrated winding one. The value for the latter is smaller because the number of slots of the motor is also smaller and skewing 1 slot would mean a too inclined winding. The

skew angle in mechanical degrees can be calculated from the skew n_{sl} given in number of slots as

$$\theta_s = \frac{360}{3pq} n_{\text{sl}}. \tag{3.4}$$

This angle is measured in the direction of rotation of the motor and should not be confused with the angle that the stator slots form with the border of the motor.

The motor torque waveforms are illustrated in Fig. 3.7. It can be seen how the ripple is substantially reduced in Motor 1 and Motor 2 when the stator is skewed. Motor 3 has, however, a much lower ripple, which corresponds to what is expected from a concentrated winding motor. Thus, the stator skew in Motor 3 further reduces the ripple, but it may not be necessary. Some texts maintain that it is not advantageous to skew a stator with concentrated windings [12]. The torque ripple reduction is most pronounced for Motor 2 which has almost a constant torque after skewing. The torque ripple values after the stator skewing are calculated as

$$\frac{\triangle T}{T_{\text{mean}}} \cdot 100 \tag{3.5}$$

and are reported in Table 3.3. A larger skew may be chosen for Motor 1 if the ripple

Table 3.3: Torque ripple values at rated torque and speed.

	n_{sl}	θ_s	Ripple without skew (%)	Ripple with skew (%)
Motor 1	1	3.8°	21.0	7.7
Motor 2	1	4.6°	29.5	0.4
Motor 3	0.33	4°	2.0	0.1

should be further reduced. A skew of 1 slot in this motor corresponds to a lower skewing angle than in Motor 2 due to the higher number of slots of the first.

3.5.2 Magnetic field

To check whether the magnets are operating in the reversible magnetization zone or, on the other hand, there is a possible risk for permanent demagnetization, the magnetic field intensity H in the magnets needs to be evaluated. Since the maximum value of H will occur at the maximum value of current applied, that is the value for which the field is evaluated. Fig. 3.8 shows the values of the magnetic field intensity along the magnets for all three motors.

The steps seen in the magnetic field intensity are created by the contribution of the different coils to the field. The interesting value is the minimum H for each case. That is the value of the demagnetizing field that the magnets must withstand. Comparing this value for each motor with the demagnetization curves of the magnets used in Fig. 3.3, the

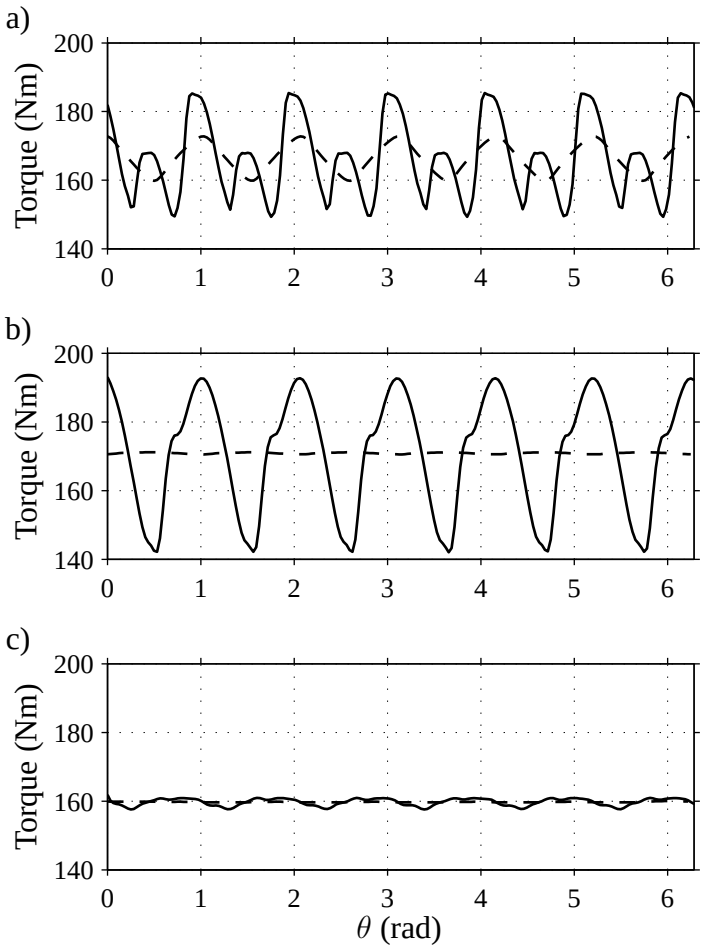

Fig. 3.7 Torque-electrical angle curves without skew (solid lines) and with skew (dashed lines) of the motors in consideration: a) Motor 1; b) Motor 2; c) Motor 3. Motors 1, 2 and 3 are skewed 1, 1 and 1/3 slots, respectively.

temperature at which the magnets will enter in the irreversible demagnetization area can be obtained. The comparison is made in Table 3.4 in which it can be seen that Motor 2 can withstand higher magnet temperatures than the others.

The thermal analysis in Chapter 4 has to confirm that these temperatures are not achieved in the magnets in any case in order to preserve their magnetic properties.

3.5.3 Losses

The motor losses are a very important aspect to consider during the design. It is necessary to compute them for the thermal simulations in Chapter 4 which will determine if the motors can withstand the resulting temperatures. The motor losses can be divided into three types: copper, magnet and iron losses.

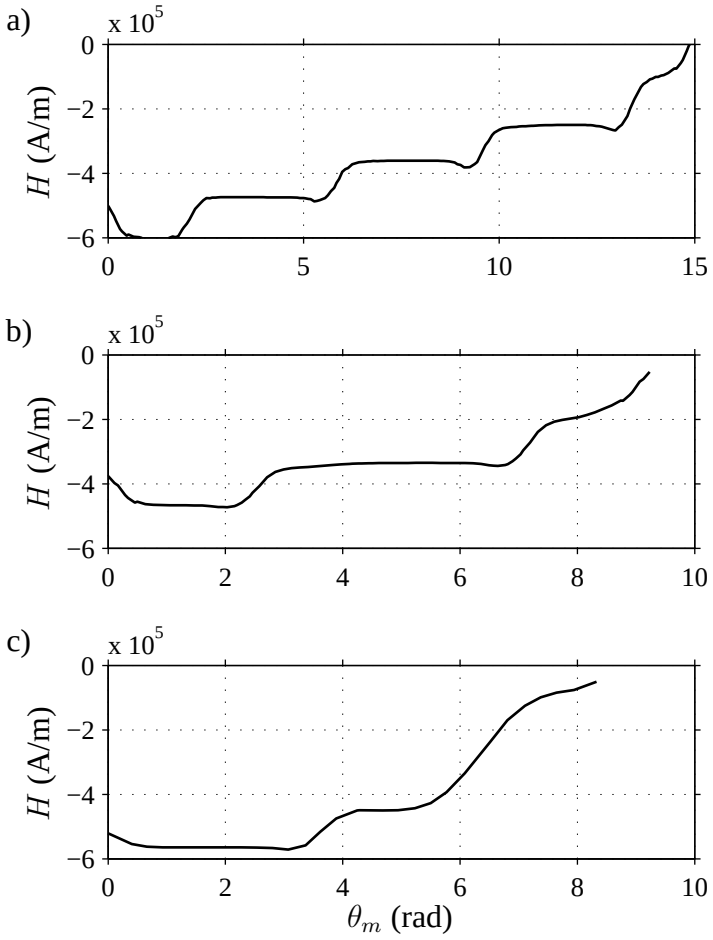

Fig. 3.8 Magnetic field intensity along one magnet at rated torque of the motors in consideration: a) Motor 1; b) Motor 2; c) Motor 3.

Copper losses

Copper losses are presented in Table 3.5 and compared with the values obtained in the analytical model. It can be seen that both results agree perfectly.

Magnet losses

The losses in the magnets occur due to the eddy currents induced. Since they are made of a conductive material, when the magnets are exposed to a variable magnetic field, currents are induced in them causing resistive losses. These magnet eddy currents are shown in Fig. 3.9. It can be seen that they are distributed differently in each motor. Every slot opening causes a flux distortion that divides the induced currents into different paths which define a closed loop. It can be seen that Motor 1 has four separated current paths while Motor 2 has two and Motor 3 has only one. From the magnet loss results obtained

Table 3.4: Maximum values of the demagnetizing magnetic field and correspondent temperature for irreversible demagnetization. The temperatures are approximated to the first available curve in which the magnet is in the reversible area.

	H_{max} (kA/m)	Demagnetizing temperature (°C)
Motor 1	-600	120
Motor 2	-475	150
Motor 3	-575	120

Table 3.5: Copper losses at rated torque.

	FEM	Analytical
Motor 1	1091 W	1090 W
Motor 2	757 W	760 W
Motor 3	1210 W	1210 W

which are presented in Table 3.6, it can be deduced that the more current paths that are created, the lower the losses. Apparently, this path subdivision seems to act as a magnet radial segmentation that reduces the losses.

Table 3.6: Magnet losses at rated torque and different speeds.

Speed	100 rpm	850 rpm	1100 rpm	1872 rpm
Motor 1	0 W	21 W	34 W	84 W
Motor 2	0 W	32 W	53 W	117 W
Motor 3	5 W	363 W	601 W	1455 W

Moreover, analyzing the magnet loss values, it can be appreciated that the concentrated windings motor has much higher magnet losses than the distributed windings configurations. This can be explained attending to the flux density in the magnets. It is known that its fundamental, due to the magnet itself, does not generate any eddy currents. Thus, the critical aspect for the eddy currents are the flux harmonics in the magnets. Fig. 3.10 shows the magnetic flux density at a point in the middle of the magnet. Its Fast Fourier Transformation (FFT) analysis is shown in Fig. 3.11. Note that the FFT graph has been zoomed in and the fundamental is not completely shown. It can be seen that the amount of harmonics in the concentrated windings motor is much higher than in the distributed windings motors. This explains the big difference in the eddy current distribution shown in Fig. 3.9 between the two types of motors and, thus, the difference in the losses.

From Fig. 3.11, the dominating harmonics of the flux density in the magnets caused by the stator slots can also be seen. The 12th and 6th harmonics are dominating in Motor 1 and Motor 2, respectively, while in the concentrated winding motor (Motor 3) the 2nd order is dominating. This matches with the cogging frequencies: $12f$ for Motor 1, $6f$ for Motor 2 and $2.1f$ for Motor 3, which are obtained from (3.6).

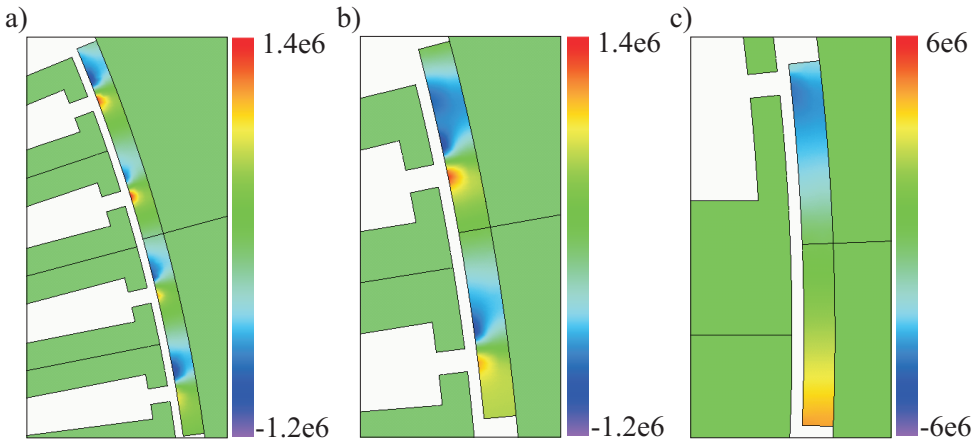

Fig. 3.9 Magnet current density (A/m^2) axial component at rated torque and speed in the motors in consideration: a) Motor 1; b) Motor 2; c) Motor 3.

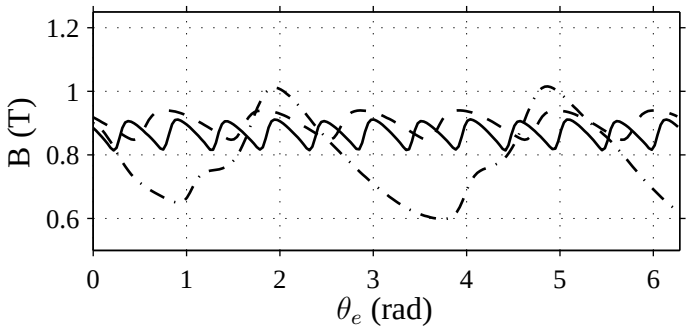

Fig. 3.10 Magnetic flux density in the middle point of the magnet at rated torque and speed in Motor 1 (solid line), Motor 2 (dashed line) and Motor 3 (dashed-dotted line).

As mentioned before, the magnets are one of the thermally critical points of the motor. Their temperature has to be carefully controlled in order to maintain them in an appropriate operating point and avoid irreversible demagnetization. Therefore, it is important to reduce their losses, which are transformed into heat, as much as possible. In this case, magnet segmentation is applied to reduce the induced eddy currents.

Despite the results obtained in the FEM simulations correspond to the motors without segmentations, they can be adjusted with an analytical model provided in [5]. According to this model, when the skin effect is negligible and only axial segmentation is taken into account, the average eddy current losses in magnets of one pole can be assumed to obey the following proportionality

$$P_{\text{eddy}} \propto \frac{1}{1 + (w/l)^2} \tag{3.6}$$

where w is the magnet segment width and l is the magnet segment length.

To apply this model for eddy-current loss prediction, it is necessary to verify that

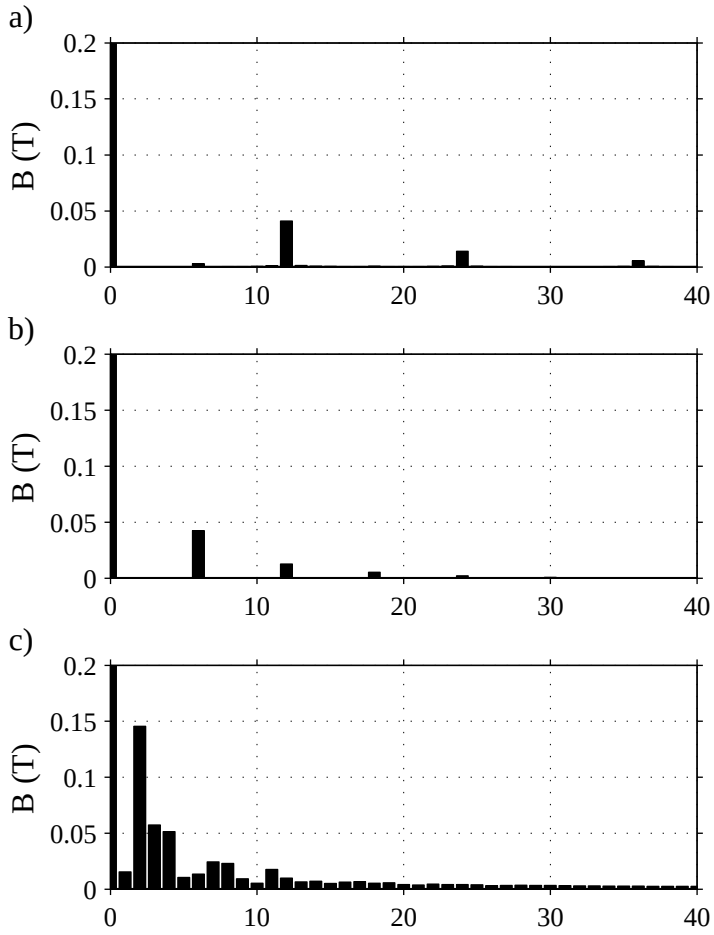

Fig. 3.11 FFT analysis of the magnetic flux density waveforms in Fig. 3.10: a) Motor 1; b) Motor 2; c) Motor 3.

the skin effect is negligible. To do this, the skin depth δ_{skin} of the magnetic material is calculated as

$$\delta_{\text{skin}} = \sqrt{\frac{2\rho}{\omega\mu}} \tag{3.7}$$

where ω is the angular frequency of the current, ρ is the resistivity and μ the permeability of the material. Now, if $w/2 < \delta_{\text{skin}}$ and $l/2 < \delta_{\text{skin}}$, the skin effect can be assumed to be negligible.

With the magnet properties described in Table 3.2 and the magnet sizes for every motor, the skin depth at rated speed in the magnets is calculated. All the values are presented in Table 3.7. From the skin depths obtained and applying the conditions previously stated, the model can be used for Motor 2 and Motor 3. For these two motors, the magnet losses obtained in the FEM simulations can, hence, be adjusted to the case with magnet

Table 3.7: Skin depth and values for its calculation.

	w (mm)	l (mm)	f_s (Hz)	f_r (Hz)	δ (mm)
Motor 1	52	30	113.33	1360	16.3
Motor 2	32.8	30	184.16	1105	18.1
Motor 3	30.6	30	198.33	425	29.2

segmentation as described in (3.8).

$$P_{\text{seg}} = \frac{1 + (w_0/l_0)^2}{1 + (w/l)^2} P_0 \tag{3.8}$$

where the subscript 0 indicates the values without segmentation. The resulting magnet losses with axial segmentation are resumed in Table 3.8 where N_Z is the number of magnet segments per pole. These results show that by applying the axial segmentation tech-

Table 3.8: Magnet losses at rated torque and speed with axial segmentation.

N_Z	1	2	3	4	5	6
Motor 2	32 W	14 W	8 W	5 W	3 W	2 W
Motor 3	363 W	160 W	90 W	57 W	40 W	29 W

nique modeled in [5], the magnet losses can be reduced by more than ten times.

Iron losses

The iron losses of the motor are produced in the stator and the rotor. The stator losses are presented in Table 3.9, where Joule losses due to eddy currents and hysteresis losses are separated. From the results, it can be seen that at low speeds, hysteresis losses are

Table 3.9: Stator losses at rated torque with sinusoidal currents.

Speed (rpm)	100		850		1100		1872	
Loss (W)	Joule	Hyst.	Joule	Hyst.	Joule	Hyst.	Joule	Hyst.
Motor 1	1	4	53	34	83	44	115	52
Motor 2	1	5	89	42	140	55	228	84
Motor 3	1	4	57	32	89	41	204	61

the most important and at higher speeds, Joule losses are dominating. Comparing the results at rated torque and speed with the ones obtained with analytical calculations in Table 2.6, it can be seen that higher values are obtained through the FEM method but that the analytical results are acceptably approximate. Moreover, Motor 2 has the highest stator losses as it was predicted by the analytical method.

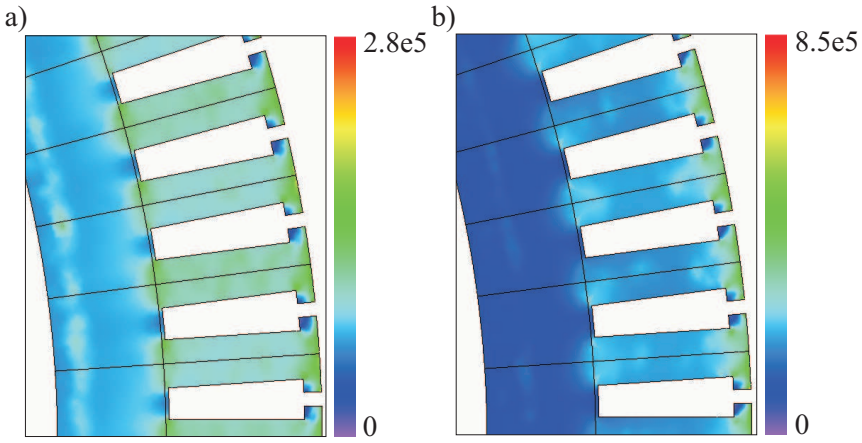

Fig. 3.12 Stator losses (W/m^3) in Motor 1 fed with sinusoidal currents at different operating conditions: a) Rated torque and speed; b) Maximum torque and speed.

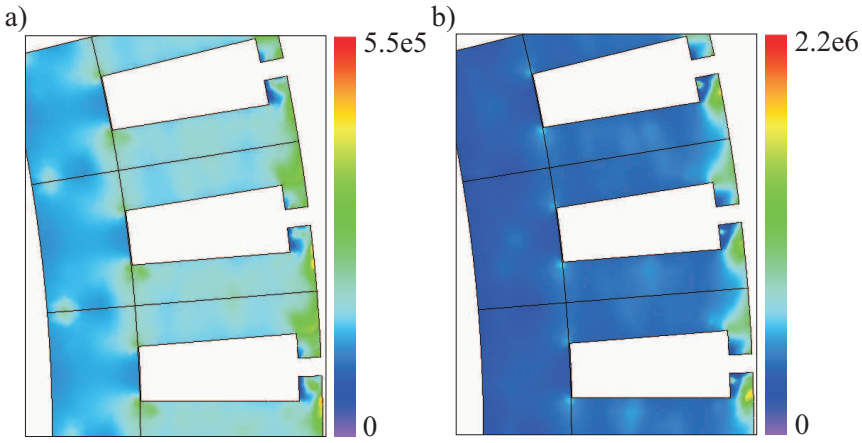

Fig. 3.13 Stator losses (W/m^3) in Motor 2 fed with sinusoidal currents at different operating conditions: a) Rated torque and speed; b) Maximum torque and speed.

Figs. 3.12, 3.13 and 3.14 show a distribution of the iron losses in the stator of Motor 1, Motor 2 and Motor 3, respectively, at two different operating conditions. It can be seen that the losses are concentrated in the stator teeth where the magnetic flux suffers the highest variations. In all three motors, the largest losses occur in the teeth at the stator's outer border. However, the concentrated winding motor appears to have a different loss distribution than the distributed winding motors. Since its teeth are so wide, there is not such a pronounced loss concentration on them as there is in the latter motors. A higher loss density area in the stator yoke under the slots is also seen in the concentrated winding motor which in the distributed winding motors corresponds to a low loss area.

The rotor losses, which are presented in in Table 3.10, are considerably higher in the concentrated winding motor than in the distributed winding configurations. As for the magnet losses, the harmonics induced in the rotor of this motor are much higher and, thus, the losses are also higher.

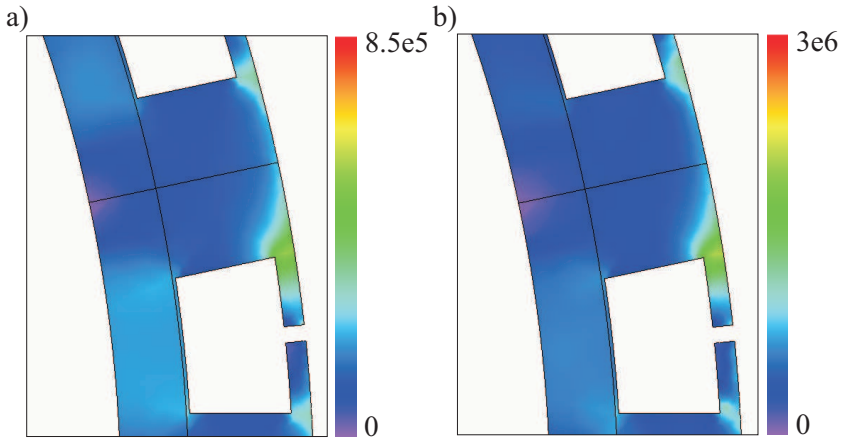

Fig. 3.14 Stator losses (W/m^3) in Motor 3 fed with sinusoidal currents at different operating conditions: a) Rated torque and speed; b) Maximum torque and speed.

Table 3.10: Rotor losses at rated torque with sinusoidal currents.

Speed (rpm)	100	850	1100	1872
Motor 1	0 W	4 W	7 W	6 W
Motor 2	0 W	3 W	4 W	7 W
Motor 3	1 W	14 W	22 W	65 W

The rotor iron loss distributions of the three motors are presented in Figs. 3.15, 3.16 and 3.17. Figs. 3.15 and 3.16, corresponding to Motor 1 and Motor 2 respectively, show a certain rotor area in which the losses are much higher than in the remaining parts. When this high loss density zone is compared with the magnetic flux density lines on the right hand pictures, it can be seen that it corresponds to an area where the flux has a bigger direction change. This flux variation can explain why the rotor losses are concentrated in that concrete areas. On the other hand, the concentrated winding motor has a smoother rotor loss distribution, but comparing Fig. 3.17a) and Fig. 3.17b) it still can be appreciated that the highest loss densities correspond to the parts where the flux has its biggest variations.

3.6 FEM simulation with PWM currents

As the motors will be fed with voltages produced by a PWM inverter, it is interesting to see how the harmonics presented in these currents will affect the motor functioning. Thus, in this section, the effect of PWM currents will be compared with the results obtained previously using pure sinusoidal currents.

Remark: The concentrated windings PMSM (Motor 3) has not been studied under PWM currents due to the extremely time demanding simulations required to obtain acceptably accurate results. The small grade of symmetry in this motor makes it necessary

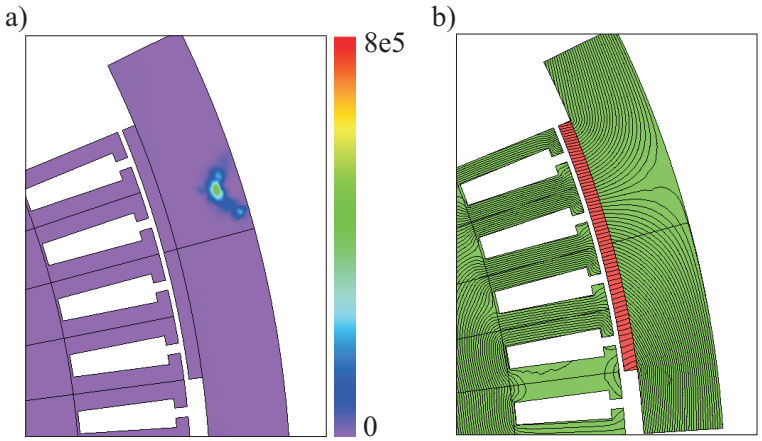

Fig. 3.15 a) Rotor losses (W/m^3) in Motor 1 fed with sinusoidal currents at rated torque and speed; b) Magnetic flux lines in Motor 1.

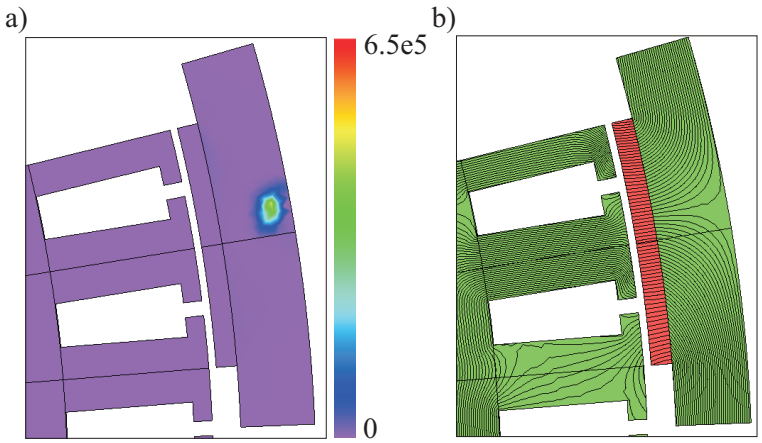

Fig. 3.16 a) Rotor losses (W/m^3) in Motor 2 fed with sinusoidal currents at rated torque and speed; b) Magnetic flux lines in Motor 2.

to simulate half of the motor model. This results in simulations that last approximately 14 times longer than the simulations of the distributed windings motors.

3.6.1 Transient model of a PM motor

To simulate the behavior of the motor when fed with currents from a PWM voltage source, a transient model of the PM motor has been implemented using Matlab/Simulink[3]. This is since no access was given to carrying out transient simulations in JMAG. The transient model used takes into account the stator skew of the motor as well as flux linkage harmonics. Cross coupling is, however, neglected.

[3]Matlab and Simulink are registered trademarks of The MathWorks Inc.

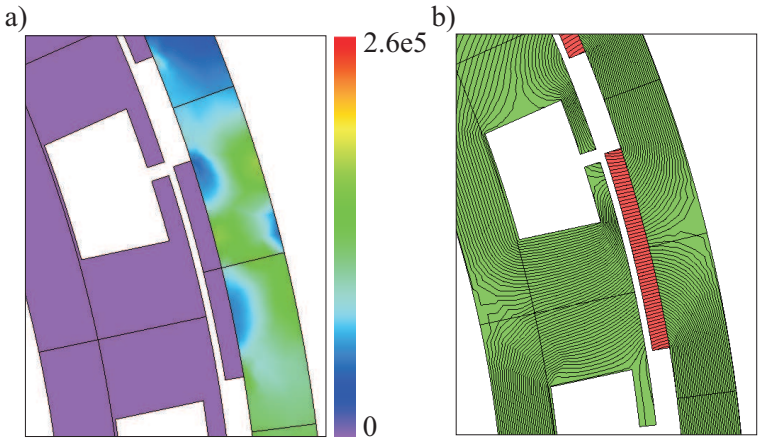

Fig. 3.17 a) Rotor losses (W/m^3) in Motor 3 fed with sinusoidal currents at rated torque and speed; b) Magnetic flux lines in Motor 3.

The motor voltage transient equations can be written as

$$u_d = R_s i_d + \frac{d\psi_d}{dt} - \omega_r \psi_q \tag{3.9}$$

$$u_q = R_s i_q + \frac{d\psi_q}{dt} + \omega_r \psi_d \tag{3.10}$$

where $\psi_d = f_d(i_d, i_q)$ and $\psi_q = f_q(i_d, i_q)$ [3]. Neglecting cross coupling, the model is simplified having $\psi_d = f_d(i_d)$ and $\psi_q = f_q(i_q)$. The flux linkages can be expressed as

$$\psi_d = \psi_{d,1} + \psi_{d,6} \cos 6\theta + \psi_{d,12} \cos 12\theta + ... \tag{3.11}$$

$$\psi_q = \psi_{q,6} \sin 6\theta + \psi_{q,12} \sin 12\theta + ... \tag{3.12}$$

where $\psi_{d,1}$ corresponds to the fundamental permanent-magnet flux linkage ψ_m at no load. To incorporate the effect of flux-linkage harmonics, the dq-current components can be calculated as

$$i_d = f_d \left(\psi_d - \sum_{i=6,12,..,}^{N} \psi_{d,i} \cos\left(i\theta + \phi_{d,i}\right) \right) \tag{3.13}$$

$$i_q = f_q \left(\psi_q - \sum_{i=6,12,..,}^{N} \psi_{q,i} \sin\left(i\theta + \phi_{q,i}\right) \right) \tag{3.14}$$

where N is the highest number of the harmonics that are taken into consideration.

In order to compute the flux linkage harmonics, the motors are simulated at no load and the phase fluxes ψ_a, ψ_b and ψ_c are obtained. To account for the motor stator skew, these phase fluxes are skewed as described in (3.3). Then, applying the amplitude-invariant Park transformation to the skewed fluxes, they are expressed in the dq-reference frame. Fig. 3.18a) shows how they are smoothened when the stator is skewed. It can also be seen that the fundamental is somewhat reduced.

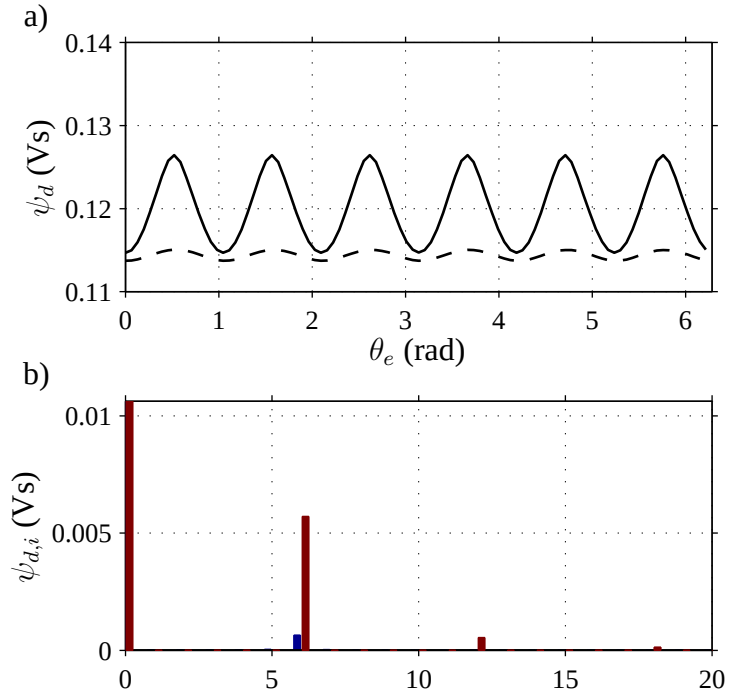

Fig. 3.18 Motor 2 flux linkage d-component: a) ψ_d without skewed stator (solid line) and with skewed stator (dashed line); b) Fast Fourier Transformation (FFT) of the fluxes ψ_d without skewed stator (brown) and with skewed stator (blue).

Once obtained the flux linkages in the dq-reference frame, an FFT analysis is conducted to compute the different harmonics. An example of this is presented in Fig. 3.18b) where the harmonic content of the flux ψ_d in Motor 2 with and without stator skew is compared. Note that the graphic is zoomed in and the fundamental component is not completely shown. The values of the main flux harmonics and their phases are presented in Table 3.11. Eqs. (3.9), (3.10), (3.13) and (3.14) can be implemented in Matlab/Simulink

Table 3.11: Flux linkage harmonics.

	$\psi_{d,6}$	$\psi_{q,6}$	$\psi_{d,12}$	$\psi_{q,12}$	$\phi_{d,6}$	$\phi_{q,6}$	$\phi_{d,12}$	$\phi_{q,12}$
Motor 1	0.78 mVs	2.3 mVs	0.08 mVs	0.19 mVs	174°	265°	140°	262°
Motor 2	0.74 mVs	0.98 mVs	0.03 mVs	0.04 mVs	178°	269°	177°	277°

to describe the transient behavior of the motor. A model of this is shown in Fig. 3.19. To determine the resulting currents, look-up tables of the form $i_d = f_d(\psi_d)$ and $i_q = f_q(\psi_q)$ have also been obtained by simulating the motor fluxes with different feeding current values.

With the PMSM transient model finished, a current controller is added to achieve the desired value of i_d and i_q. The controller computes the necessary voltages u_d and u_q

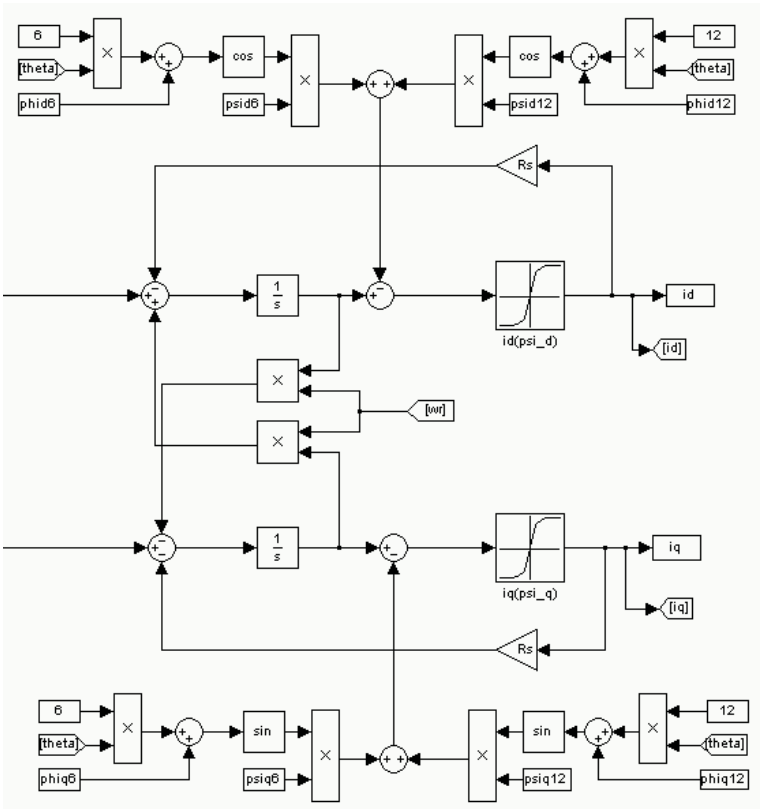

Fig. 3.19 Simulink transient PMSM model.

from the references given and the actual dq-current values. They are transformed again into a 3-phase coordinate system and given as reference to a PWM inverter that supplies the voltage to the PMSM transient model. The PWM used has a carrier frequency of 5 KHz and the dc-link voltage is 350 V. Fig. 3.20 shows the Simulink model of the current controller.

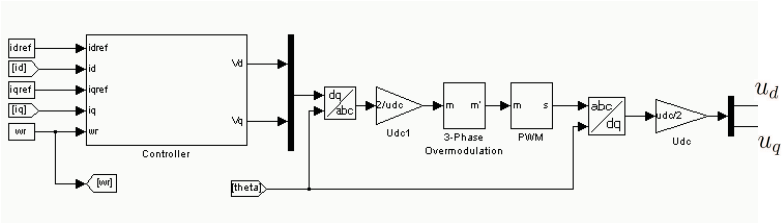

Fig. 3.20 Current controller and PWM inverter.

An example of the currents obtained with this model which are fed into the motor when the PWM technique is applied is shown in Fig. 3.21. As seen, the PWM inverter introduces an important ripple.

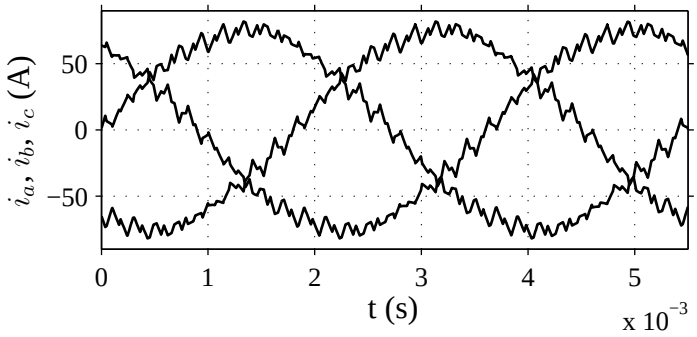

Fig. 3.21 Motor 2 PWM currents at rated torque and speed.

3.6.2 Torque

The current ripple introduced by the action of the PWM affects the torque of the motors. As it can be seen from Fig. 3.22, the torque waveform also acquires a high frequency ripple which is more clearly observed in Motor 2. This represents an inconvenient and may increase the motor noise. However, as it can be seen from the dashed lines in Fig. 3.22, this ripple can also be reduced by skewing the stator of the motor.

3.6.3 Losses

The PWM will introduce undesired harmonics that will have an effect on the motor losses. This effect is studied separately in the magnets and iron on the motor.

Copper losses

The copper losses under PWM currents are presented and compared with the values obtained with sinusoidal currents in Table 3.12. There is a not an important difference, but it still can be seen how the harmonics present in the currents increase the copper losses.

Table 3.12: Copper losses at rated torque under PWM currents.

	sinu.	PWM
Motor 1	1091 W	1092 W
Motor 2	757 W	761 W

Magnet losses

The results of the magnet losses in Motor 1 and Motor 2 when PWM currents are used is presented in Table 3.13. As done before under sinusoidal currents, the effect of magnet segmentation is considered, and the method described in [5] is applied again. Table 3.14

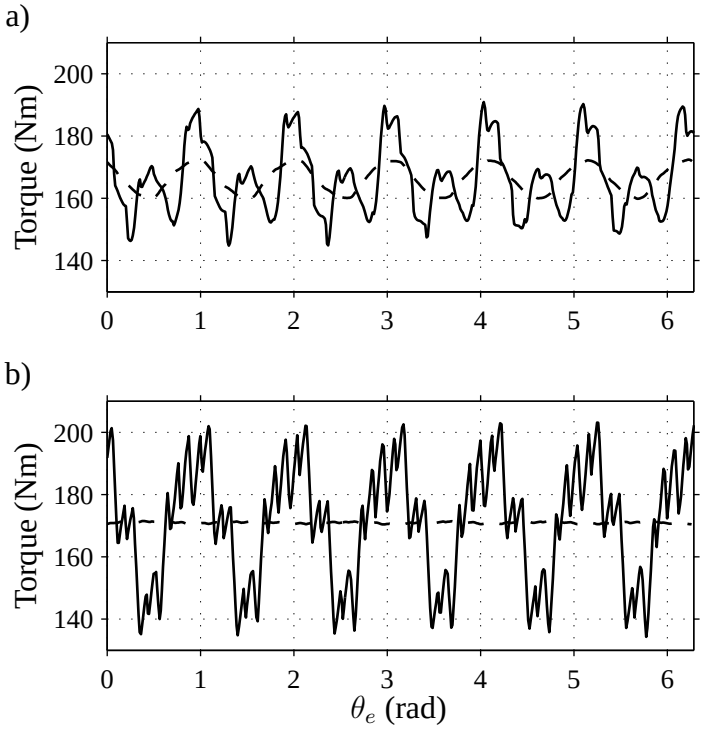

Fig. 3.22 Torque-electrical angle curves without skew (solid lines) and with skew (dashed lines) of the motors in consideration fed with PWM currents. Both, Motor 1 and Motor 2 are skewed 1 slot: a) Motor 1; b) Motor 2.

Table 3.13: Magnet losses under PWM currents at different speeds and rated torque

Speed	100 rpm	850 rpm	1100 rpm	1872 rpm
Motor 1	1 W	56 W	70 W	116 W
Motor 2	1 W	103 W	142 W	181 W

shows the results of the magnet losses when different number of axial magnet segments are considered.

The current density that causes the magnet losses with PWM currents is presented in Fig. 3.23. The distribution is very similar to the one observed in the case of sinusoidal currents, with current paths around the slot openings, but the values are higher.

Iron losses

The stator losses under PWM currents are presented in Table 3.15. Comparing these results with the ones obtained using sinusoidal currents in Table 3.9 it can be seen that the PWM currents produce a significant increase of the stator losses due to eddy currents, but that the hysteresis losses have only barely increased.

The stator loss distribution for the motors in consideration at two different operating

Table 3.14: Magnet losses under PWM currents at rated torque and speed with axial segmentation.

N_Z	1	2	3	4	5	6
Motor 1	56 W	17 W	8 W	5 W	3 W	2 W
Motor 2	103 W	39 W	19 W	11 W	7 W	5 W

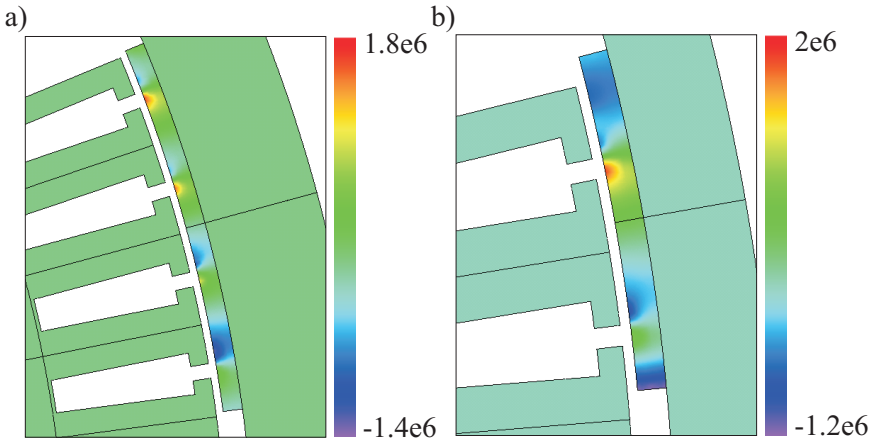

Fig. 3.23 Magnet current density (A/m^2) axial component at rated torque and speed in the motors in consideration: a) Motor 1; b) Motor 2.

conditions is presented in Figs. 3.24 and 3.25. As in the case with sinusoidal currents, the highest loss density is concentrated in the outer stator border. This effect is much more pronounced in Motor 2. Motor 1 has, however, a more distributed loss density in its teeth. A high loss density ring is also appreciated in the stator yoke of this motor which could be slightly seen also with sinusoidal currents, but that has become much more evident in this case.

Fig. 3.26 compares the Joule loss frequency distribution in the stator of Motor 2 with sinusoidal currents and PWM currents. Again, note that the graph is zoomed in and the fundamental is not completely shown. It can be appreciated that the basic frequency and its harmonic components are almost the same in both graphs. However, when the motor is fed with PWM currents, the PWM basic frequency (5 kHz) and its harmonics are also involved. This is the reason for the loss increase produced.

The rotor losses with PWM currents at different speeds are reported in Table 3.16. When comparing them to the rotor losses with sinusoidal currents, it is seen that they are around six times higher. This shows that the loss increase in the rotor due to the action of the PWM is proportionally much bigger than the one produced in the stator of the motors. The combination of time harmonics, introduced by the PWM, and space harmonics, introduced in the rotor by the stator slots, is the reason for this increase.

Figs. 3.27 and 3.28 show the rotor loss distribution and the magnetic flux lines of the motors in consideration. The results are similar to the ones obtained with sinusoidal

Table 3.15: Stator losses at rated torque with PWM currents.

Speed [rpm]	100		850		1100		1872	
Loss [W]	Joule	Hyst.	Joule	Hyst.	Joule	Hyst.	Joule	Hyst.
Motor 1	1	4	77	35	125	45	174	52
Motor 2	2	5	152	43	219	55	372	88

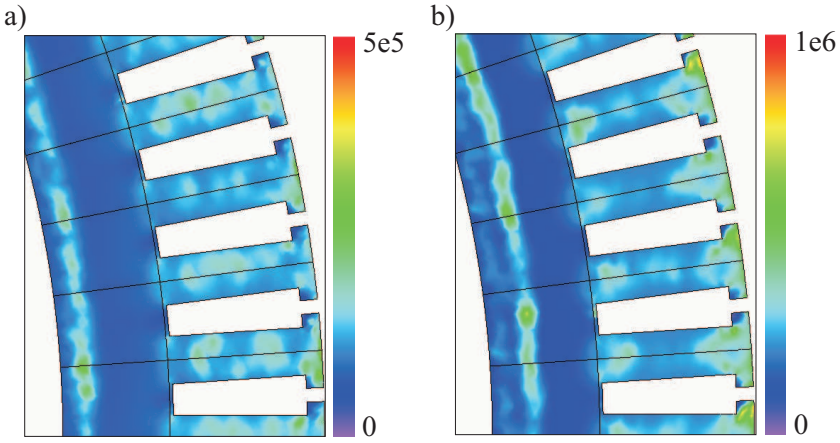

Fig. 3.24 Stator losses (W/m^3) in Motor 1 fed with PWM currents at different operating conditions: a) Rated torque and speed; b) Maximum torque and speed.

currents. The high density loss area matches with the flux lines that have the biggest variations.

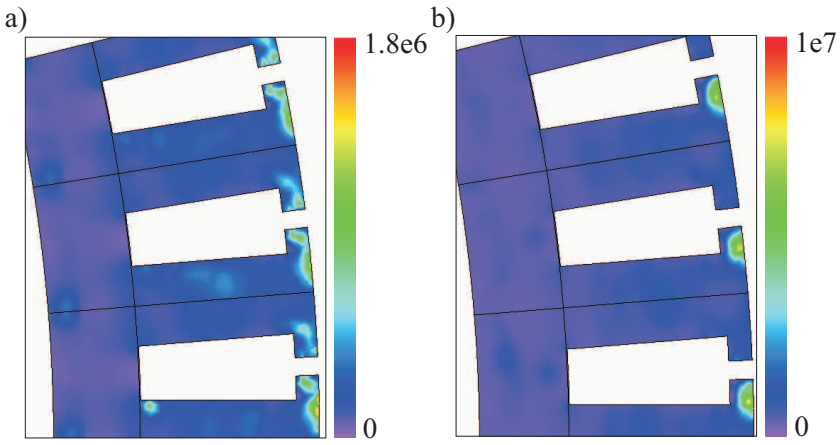

Fig. 3.25 Stator losses (W/m^3) in Motor 2 fed with PWM currents at different operating conditions: a) Rated torque and speed; b) Maximum torque and speed.

Table 3.16: Rotor losses at rated torque with PWM currents.

Speed (rpm)	100	850	1100	1872
Motor 1	0 W	24 W	30 W	35 W
Motor 2	0 W	17 W	20 W	47 W

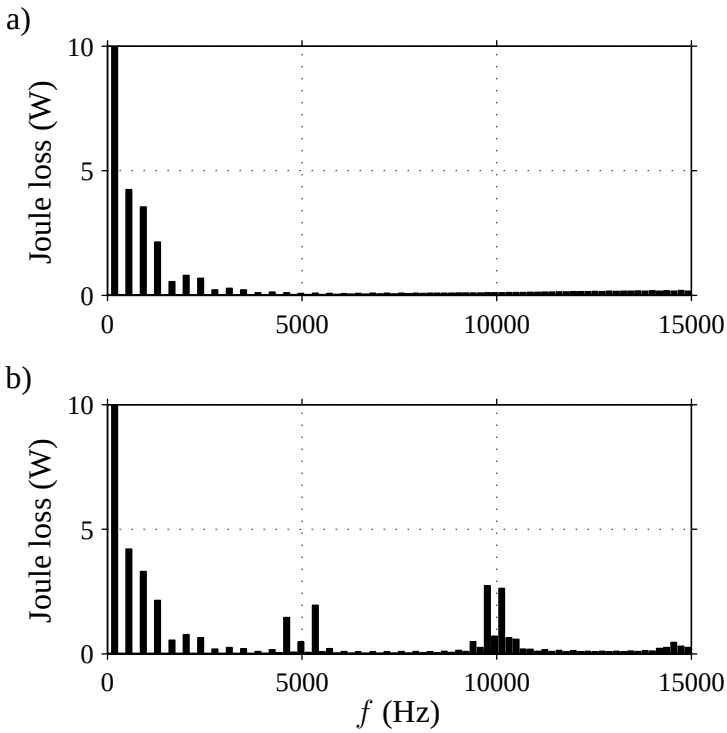

Fig. 3.26 Joule loss frequency component of stator core in Motor 2 at rated torque and speed: a) Sinusoidal currents; b) PWM currents.

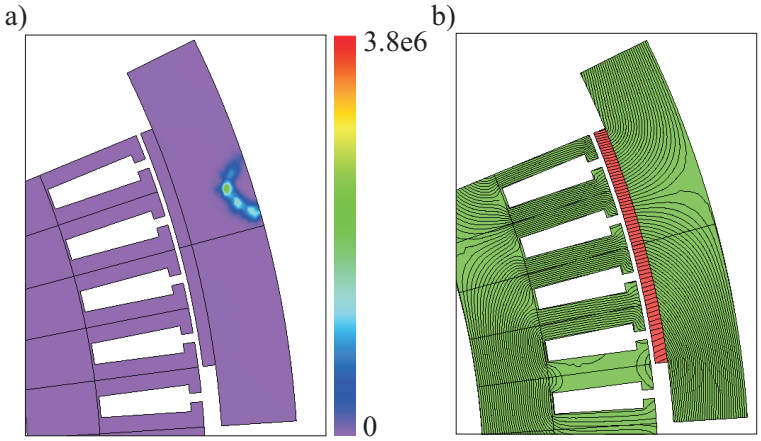

Fig. 3.27 a) Rotor losses (W/m^3) in Motor 1 fed with PWM currents at rated torque and speed; b) Magnetic flux lines in Motor 1 at rated torque and speed.

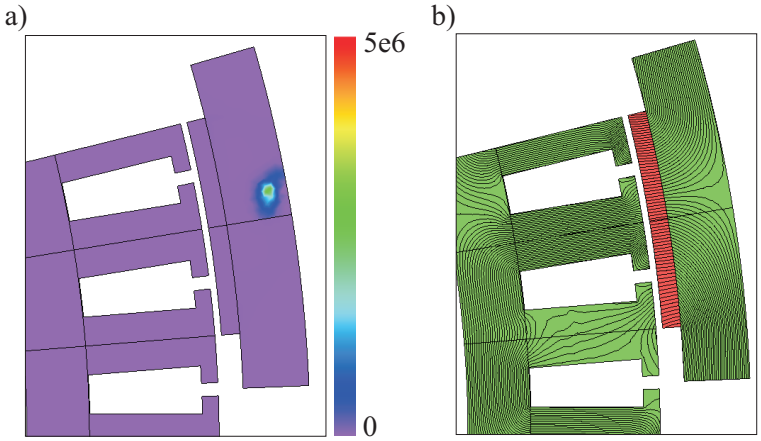

Fig. 3.28 a) Rotor losses (W/m^3) in Motor 2 fed with PWM currents at rated torque and speed; b) Magnetic flux lines in Motor 2 at rated torque and speed.

Chapter 4

Thermal analysis

In this chapter, a thermal analysis of the motors presented and studied in the previous chapters is carried out. The models used for the different parts, settings and parameters are presented and discussed. Finally, the results of the analysis are shown and the achieved temperatures are contrasted with the material properties.

4.1 Initial considerations

The thermal software used to run this thermal analysis is Motor-CAD[1] which is based on analytical lumped-circuit analysis. Therefore, it provides analytical results of the temperatures that the motor would achieve in different nodes set along the motor. The calculations are in this way much quicker than if a FEM calculation was carried out. The models described in this chapter use correlations that are based on certain dimensionless numbers used in heat and mass transfer. These numbers are reviewed in Appendix C.

The model is set to be surrounded by air, both in the outer an inner parts. The ambient temperature is set to 40 ^{o}C which is the maximum ambient typical temperature when designing motors [15].

4.2 Geometry model

The motors are modeled independently and considering an approximate housing. There are also some aspects of the motor placement that are not considered due to their difficulty to be modeled. As an in-wheel motor, and as it can be deduced from the picture model provided in Fig. 4.1, components such as brakes and the suspension are placed inside the wheel. These components will have an effect on the heat transmission which, in this case, is neglected. Of particular importance may be the omission of the brakes which will dissipate an important amount of heat during operation. However, the motor duty cycles

[1]Motor-CAD is a registered trademark of Motor Design Ltd.

extracted from the driving cycles has been calculated as if the only braking was made with the motor.

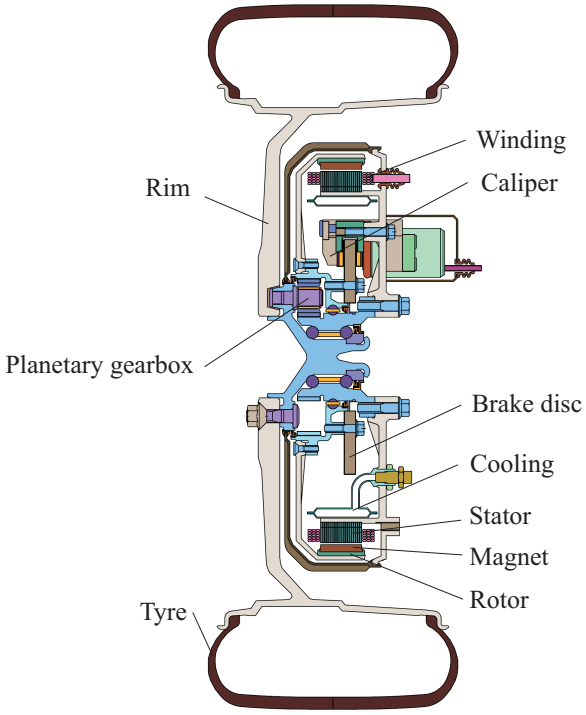

Fig. 4.1 In-wheel motor design proposal.

The motor radial cross sections are modeled with the exact shape and dimensions of the ones used in the FEM simulations in Chapter 3, which were originally obtained from the analytical solutions in Chapter 2, with the addition of the housing and a cooling groove.

The axial cross section of the models does not offer many differences. The stator, rotor and magnets have an axial length of 30 mm which is set in the motor characteristics. The only remarkable difference between the three motors and with the analytical design is the length of the windings overhang.

As explained in [12], the end winding overhang of a concentrated winding motor is much shorter than the one of a distributed windings motor. Furthermore, there is also a significant reduction in a double layer concentrated winding compared to a single layer winding. However, in this case, the concentrated windings motor has a much higher number of turns per slot (27) than the distributed winding motors (11 and 10 for Motor 1 and Motor 2, respectively), a fact that will make the volume of the winding overhang increase in the first motor respect to the others. It has also been taken into account that Motor 1 has 2 slots per pole and phase and, thus, its end windings will have approximately twice the volume of the ones in Motor 2 ($q = 1$). Thus, Motor 1 and Motor 3 are modeled with a winding overhang of 20 mm per side and Motor 2 with 20 mm per side and an outer

expansion of 20 mm in the radial direction equally divided between the inner and outer directions.

The total length of the motor with its housing is in all three cases set to 90 mm, which matches the space available inside the wheels of the vehicle.

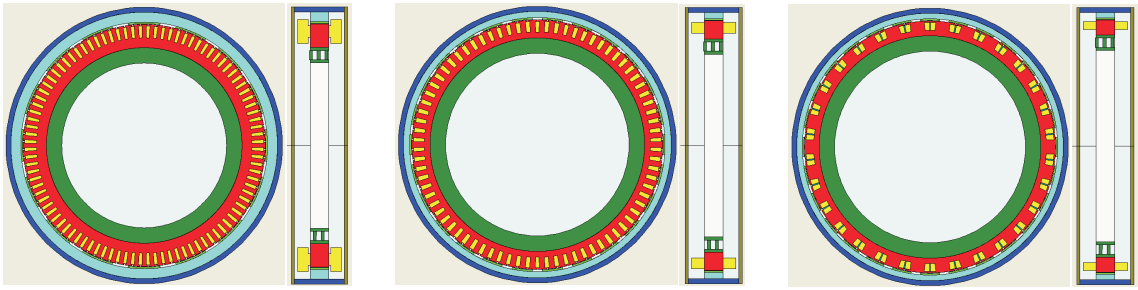

Fig. 4.2 Radial and axial cross sections of the models of Motor 1, Motor 2 and Motor 3.

4.3 Winding model

The winding model is a layered based model in which the conductors with a similar temperature are modeled as one layer. A more detailed description of it is given in [17]. Some parameters selected in the model are presented in Table 4.1. The slot insulation thickness is according to [15] normally between 0.2 and 0.5 mm. Thereby, a 0.2 mm thick liner is used, keeping the value used in the analytical model. The wire and copper diameters are chosen to adjust the copper area to the one calculated in the analytical model and the end winding slot fill is set to the same value as in the slots.

Table 4.1: Winding model parameters.

	Motor 1	Motor 2	Motor 3
Winding type	Overlap.	Overlap.	Non overlap.
Conductors/slot	11	10	27
Wire diameter (mm)	2.83	3.17	2.99
Copper diameter (mm)	2.74	3.08	2.9
Liner thickness (mm)	0.2	0.2	0.2
Impregnation goodness	0.8	0.8	0.8

There is no extra insulation in the slot base or tooth sides and the copper penetrates down to the bottom of the slot. The impregnation goodness is a factor set to account for imperfections in the impregnation material such as air pockets. The value is equally set to 0.8 in the slots and end windings. Higher values could be achieved using vacuum methods.

4.4 Air gap model

The heat transfer across the motor air gap includes conduction, convection and radiation. Radiation is separately studied but the conduction and convection heat flows have to be evaluated depending on the state of air. Three states are distinguished in Motor-CAD based on the results obtained by Taylor [18]. A laminar state under a certain $Re_{\text{vort.}}$, where the heat transfer is purely conductive, a state where the flow has a regular vortex pattern in which the heat transfer increases and a turbulent state over $Re_{\text{turb.}}$, where it increases further.

Laminar $(Re < Re_{\text{vort.}})$:

$$Nu = 2 \tag{4.1}$$

Vortex $(Re_{\text{vort.}} < Re < Re_{\text{turb.}})$:

$$Nu = 0.212 \left(Re \left(\frac{\delta}{r_\delta} \right)^{0.5} \right)^{0.63} Pr^{0.27} \tag{4.2}$$

Turbulent $(Re > Re_{\text{turb.}})$:

$$Nu = 0.386 \left(Re \left(\frac{\delta}{r_\delta} \right)^{0.5} \right)^{0.5} Pr^{0.27}. \tag{4.3}$$

The stator slots and the magnets will, however, affect the heat transfer, adding irregularities to the surfaces. Tests made by Gazley [2] suggest that the heat transfer is reduced in the laminar flow (around 20 % for stator and rotor slots), maintained in the vortex flow and increases in the turbulent flow. By calculating the Reynolds number in the air gap and checking the regimen obtained for the motors in consideration, it is seen that the critical speeds for changing to the different air states are around 550 rpm from laminar to vortex flow and 1400 rpm from vortex to turbulent flows. The calculations are made using the air temperatures at 80 ºC.

To account for the slotting effect, an air gap conductivity multiplier can be modified in order to increase/decrease the heat transmission through it. Thus, the multiplier is decreased or increased to reduce or enhance the heat transmission respectively depending on the motor speed. At rated speed, the value is set to 1 but it is modified up to 20 % depending on the motor speed.

4.5 End space model

The end space is defined as the area within the end shields that contains the end windings [17]. It is a complex area to model due to the air flow that is generated in it. This air

flow varies considerably with the end windings shape and is, thus, difficult to predict. The formulation used in Motor-CAD is given by

$$h = k_1 \left(1 + k_2 v^{k_3}\right) \tag{4.4}$$

where h is the heat transfer coefficient, k_1 is a coefficient that accounts for natural convection, k_2 and k_3 are coefficients that adjust the forced convection due to the rotation of the motor and v is the fluids local velocity. Different authors have published values for these coefficients and Schubert values have been chosen in this case.

4.6 Housing surfaces model

Since the motors in consideration are of the outer rotor type, the housing will rotate together with the rotor of the motor. As seen from the model provided in Fig. 4.1, the front end cap is attached to the housing, but the rear end cap is not, and, thus, will not rotate. This rotation to which some of the outer parts of the motor are subjected makes that the heat transfer is produced by both natural and forced convection. Motor-CAD uses a formulation from [6] that combines both effects into a single heat transfer coefficient expressed as

$$h_{\text{mix}}^3 = h_{\text{forc.}}^3 \pm h_{\text{nat.}}^3 \tag{4.5}$$

being $\pm$ positive when the natural flow is transversal to or assisting the forced flow and negative if it is opposing.

4.6.1 Natural convection

Natural convection takes place in all the outer parts of the model; housing and end caps. The heat transfer coefficient for each of this parts is calculated from correlations given in Motor-CAD which are taken from [16].

The housing is modeled as an horizontal cylinder. The average Nusselt number for a horizontal cylinder of diameter D is [16]:

Laminar flow $(10^4 < Gr \cdot Pr < 10^9)$:

$$Nu_D = 0.525 \left(Gr \cdot Pr\right)^{\frac{1}{4}} \tag{4.6}$$

Turbulent flow $(10^9 < Gr \cdot Pr < 10^{12})$:

$$Nu_D = 0.129 \left(Gr \cdot Pr\right)^{\frac{1}{3}} \tag{4.7}$$

On the other hand, the end caps are modeled as vertical flat plates. The average Nusselt number for a vertical flat plate of length L is [16]:

Laminar flow $(10^4 < Gr \cdot Pr < 10^9)$:

$$Nu_L = 0.59\,(Gr \cdot Pr)^{\frac{1}{4}} \tag{4.8}$$

Turbulent flow $(10^9 < Gr \cdot Pr < 10^{12})$:

$$Nu_L = 0.129\,(Gr \cdot Pr)^{\frac{1}{3}} \tag{4.9}$$

The heat transfer coefficient can then be calculated in both cases as

$$h = Nu\frac{\kappa}{l} \tag{4.10}$$

where κ is the air thermal conductivity and l is the characteristic length, D and L in each case.

Motor-CAD computes the properties of air at the operating conditions and applies the laminar or turbulent equation according to the regimen obtained.

4.6.2 Forced convection

For the forced convection the housing and the front end cap are considered, but as mentioned before, not the rear end cap. Both, housing and end cap are modeled as a flat plate. The housing correlation is modeled with this geometry because of the similarity between the movement of the surface of the housing with standing air and a standing surface with moving air. For the end cap, the air velocity is considered an average of the air velocities in its surface, i.e. $0.5w$. The average Nusselt number is obtained using a correlation given in [6]:

Laminar flow $(Re < 5 \cdot 10^5)$ and $(0.6 < Pr < 50)$:

$$Nu = 0.664\,(Re)^{0.5}\,Pr^{0.33} \tag{4.11}$$

Turbulent flow $(Re > 5 \cdot 10^5)$:

$$Nu_L = \left(0.037Re^{0.8} - 871\right)Pr^{0.33} \tag{4.12}$$

4.7 Cooling system model

The motors are cooled with a spiral groove attached to the inner part of the stator. Through this channel, a cooling liquid circulates refrigerating the motor. The cooling system will have an important influence in the motor temperatures. The selection of different inlet temperatures and flows can make them vary considerably. However, the cooling system is made for the motor and not the other way round, which makes these parameters variables to some extent. The inlet temperature will vary depending on the car radiator size and

whether the car electronics are cooled with the same system or not. The flow through the groove will also depend on the pump capacity and the pressure resistance of the channel. At first stage, an inlet temperature of 60 °C and a fluid volume flow rate of 0.05 l/s are set. Depending on the resulting motor temperatures, these parameters can be readjusted.

The cooling fluid used is Ethylene-Glycol mixed with water in a 50/50 proportion (EGW 50/50). It is chosen because of its high thermal conductivity (0.39 W/(mK) at 25 °C) and specific heat (3280 J/(kgK) at 25 °C), together with a low freezing point (-34 °C). A mix of 60/40 can also be chosen if the required freezing point is lower, only slightly sacrificing its cooling properties.

The channel has a rectangular cross section, for which Motor-CAD applies three different heat transfer correlations, obtained from [14], depending on the fluid state. Laminar flow is used for $Re < 2300$, turbulent for $Re > 3000$ and a weighted average of them in the transition state.

4.8 Materials

The results obtained in the thermal analysis depend strongly on the accuracy of the material data used to model the motor. Thus, it is important to use as exact material data as possible. Unfortunately, it is not possible to find thermal data from the steel selected and, thus, an approximate steel data is used.

The thermal conductivity of iron is a function of its silicon content. A table graph with this variation is shown in [17]. The thermal properties of the magnet used are only found in a range (κ = 5 – 15 W/(mK) and c_p = 350 – 550 J/(kgK)). The mid point of the range is selected as input for the model.

A relation of the materials used to model the different motor components and their thermal properties is presented in Table 4.2.

Table 4.2: Material thermal properties at 300 K.

Component	Material	κ (W/(mK))	c_p (J/kgK)	ρ (kg/m^3)
Stator	Iron (2% Silicon)	19	460	7600
Rotor	Iron (2% Silicon)	19	460	7600
Magnets	VACODYM 854	10	450	7700
Housing	Aluminium (Alloy 195, Cast)	168	883	2790
End cap	Aluminium (Alloy 195, Cast)	168	883	2790
Spiral groove	Aluminium (Alloy 195, Cast)	168	883	2790
Copper	Copper	401	385	8933
Wire insulation	Nylon	0.24	1600	1100
Impregnation	Nylon	0.24	1600	1100
Liner	Nylon	0.24	1600	1100

The selection of the winding insulation material is a key factor since it is the most

temperature critical component [15] apart from the permanent magnets. The insulation material chosen for this motor is class H according to the IEC 85 standard.

4.9 Contact resistance and interface gaps

The contact resistance between the different components of the motor is due to the imperfection of the material surfaces and is influenced by conditions such as the pressure, material hardness or surface smoothness [17]. Special attention has to be paid to these parameters since they sometimes influence the heat transfer more than the actual material resistances.

The method used by Motor-CAD to implement contact resistances is to calculate an equivalent interface gap. Some books like [14], provide useful tables with thermal resistance values, which can be converted to equivalent air gaps using the thermal conductivity of air (0.026 W/m/C at 300 K). However, the values of these effective air gaps vary significantly depending on the material surface finish and the pressure between the components. An added difficulty in determining the contact resistance between two components with different materials such as the steel rotor and the aluminium housing, is that they have different heat expansion coefficients, making the interface gap vary with the temperature.

The interface air gaps between the components are the same for the three motors and set using the first estimate values given in [17]. The mid point of the range given is chosen and displayed in Table 4.3.

Table 4.3: Interface air gaps.

Interface	Materials	Air gap (mm)
Stator-Spiral groove	Iron-Aluminium	0.003
Rotor-Housing	Iron-Aluminium	0.003
Rotor-Magnet	Iron-Magnet	0.003
Housing-End cap (front)	Aluminium-Aluminium	0.0012
Housing-End cap (rear)	Aluminium-Aluminium	3

The air gap between the housing and the rear end cap is set to 3 mm. This is done to adjust the model to Fig. 4.1 in which it can be seen that there is not a physical contact between those two components.

It has not been possible to find information about the contact resistance between the magnets and the rotor, so this interface was approximated as an iron-aluminium interface. The magnet coatings are not considered, but one of the possibilities described by the manufacturer is an aluminium spray coating, and, thus, this material was selected for its surface.

4.10 Radiation

The radiation heat transfer coefficient is calculated as

$$h_r = \sigma \varepsilon F_{i,j} \frac{T_i\,(\mathrm{K})^4 - T_j\,(\mathrm{K})^4}{T_i(\mathrm{K}) - T_j(\mathrm{K})} \tag{4.13}$$

where σ is the Stephan-Boltzmann constant, ε is the surface emissivity, $F_{i,j}$ is the view factor between the surfaces i and j and $T_{\text{surf.}}$ is the surface temperature. When the material radiates to the ambient, T_j is the ambient radiation temperature typically represented as T_∞. The different parameters have to be set for the surfaces exposed to radiation in the model. Both, external and internal radiation are considered. The housing and the end caps radiate to the ambient and the inner and outer rotor surfaces radiate between each other. The ambient radiation temperature is considered to be the same as the ambient temperature ($T_\infty = 40$ °C). The emissivity is a function of the material and the surface state and varies also with the temperature. The values used correspond to a temperature of 300 K and a usual surface finish. They are obtained from [6]. The view factor $F_{i,j}$ is described as the fraction of radiation leaving surface i which is intercepted by surface j [6]. The view factor in the outer surfaces radiating to the ambient is 1 and the value of between the inner and the outer air gap surface is also approximated to that value. The parameters are presented in Table 4.4 and are common for the three motors.

Table 4.4: Radiation parameters.

Surface	Material	ε	F
Housing	Aluminium	0.82	1
End cap	Aluminium	0.82	1
Air gap (inner surface)	Iron	0.22	1
Air gap (outer surface)	Iron	0.22	1

4.11 Schematic

The implementation of the geometry and the heat transfer models previously described results in the schematic presented in Fig. 4.3. The circuit represents how the heat transfer is made between the different parts of the motors. Each resistance represents a thermal resistance between components, which may be due to conduction (material and contact resistances), convection or radiation. The outer line, represents the ambient, with which many components exchange heat.

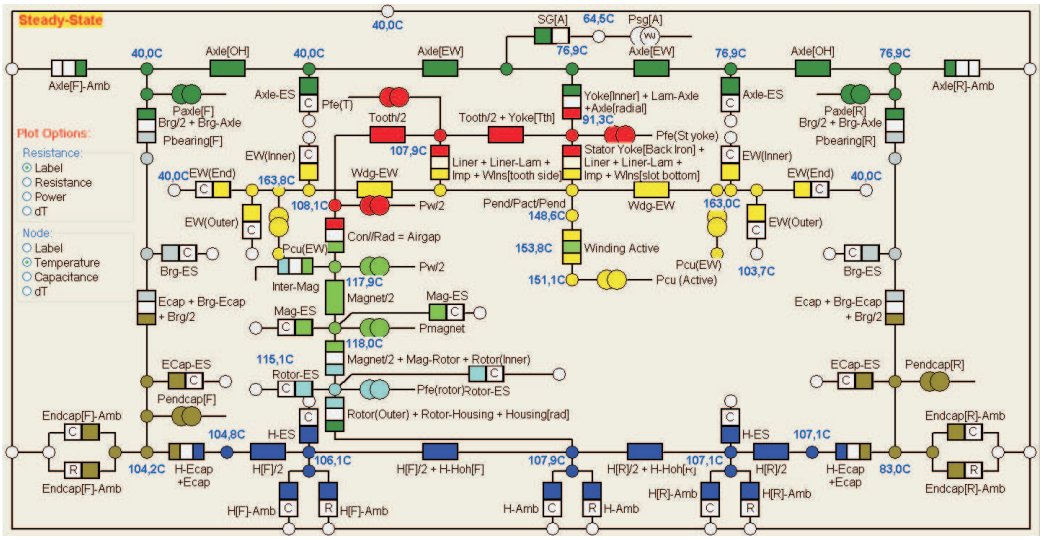

Fig. 4.3 Heat transfer schematic for Motor 3.

4.12 Losses

The motor losses at different operating conditions have been calculated in Chapter 3. However, for the thermal analysis, only the losses at one functioning condition are needed for each motor. The losses at rated torque and speed of the motors are, thus, selected. Additionally, for a better loss distribution in the thermal model, separated losses from the stator yoke and teeth are required. To obtain them, a new model is created in JMAG in which these two areas are separated and the simulations are carried out.

Under these conditions, the results of the motor losses both using sinusoidal currents and PWM currents are reported in Table 4.5. The magnet losses in the table are considered without axial segmentation. This is done to have a reasonable comparison between the three motors since the data for axial segmentation in Motor 1 could not be calculated. Moreover, not applying the axial segmentation will result in higher temperatures which means a more conservative thermal analysis. However, the results for Motor 1 and

Table 4.5: Losses (W) at rated torque and speed of the motors in consideration.

	Motor 1		Motor 2		Motor 3	
	Sinu.	PWM	Sinu.	PWM	Sinu.	PWM
Copper	1091	1092	757	761	1210	-
Stator yoke	37	46	47	61	37	-
Stator teeth	50	66	84	134	52	-
Magnets	21	56	32	103	363	-
Rotor	4	24	3	17	14	-

Motor 3 are also calculated considering the segmentation since the magnet temperatures

will be largely influenced and it is intended to be applied.

As mentioned above, the motor losses at different speeds and loads considered in the thermal analysis are based on the losses at rated conditions. Motor-CAD extrapolates these losses to obtain the losses for any motor operating point according to

$$P = P_i \left(\frac{n}{n_{\text{ref.}}} \right)^{\alpha} \tag{4.14}$$

where P_i is the reference loss at rated torque and speed and α is a coefficient that has to be adjusted for the different parts of the motor. The value of α for the three motors and their different parts is calculated to fit the simulated loss curves and presented in Table 4.6. An example of the fitting of the estimated losses to the obtained losses via FEM simulations is given in Fig. 4.4, where the curves in Motor 1 are compared. To guarantee that the losses have not been underestimated, a safety coefficient of 1.5 is applied. Thus, all the losses on Table 4.5 will be multiplied by 1.5 when running the simulations.

Table 4.6: Values of coefficient the α.

	Copper	Stator Yoke	Stator Teeth	Magnets	Rotor
Motor 1	0	1.5	1.5	1.9	2.2
Motor 2	0	1.5	1.5	1.9	2
Motor 3	0	1.5	1.5	1.9	1.9

4.13 Motor duty cycles

The driving cycles used are presented in Fig. 4.5. The first one is obtained from a real car driving in the city of Göteborg and the second one corresponds to the UDDS test. The latter is an United States Environmental Protection Agency dynamometer test on fuel economy that represents city driving conditions and is used for light duty vehicle testing. These cycles offer information about the vehicle's speed during a certain time. However, the duty cycles required to run the thermal simulation must include data from the motor torque and speed at every time.

The speed of the motor can be easily calculated from the vehicle's velocity using the wheel radius and the gearbox ratio. The torque is obtained using (B.4), deduced in Appendix B. The acceleration of the vehicle is computed by differentiating the vehicle's speed via a discrete filter. The rest of the values used for the calculations are obtained from the vehicle specifications and are presented in Table 4.7.

The resulting motor speed and torque cycles are shown in Fig. 4.6 and Fig. 4.7. The city driving test has an average motor speed of 327 rpm and a torque rms value of 91 Nm while the UDDS test has an average motor speed of 393 rpm and a torque rms value of 45 Nm.

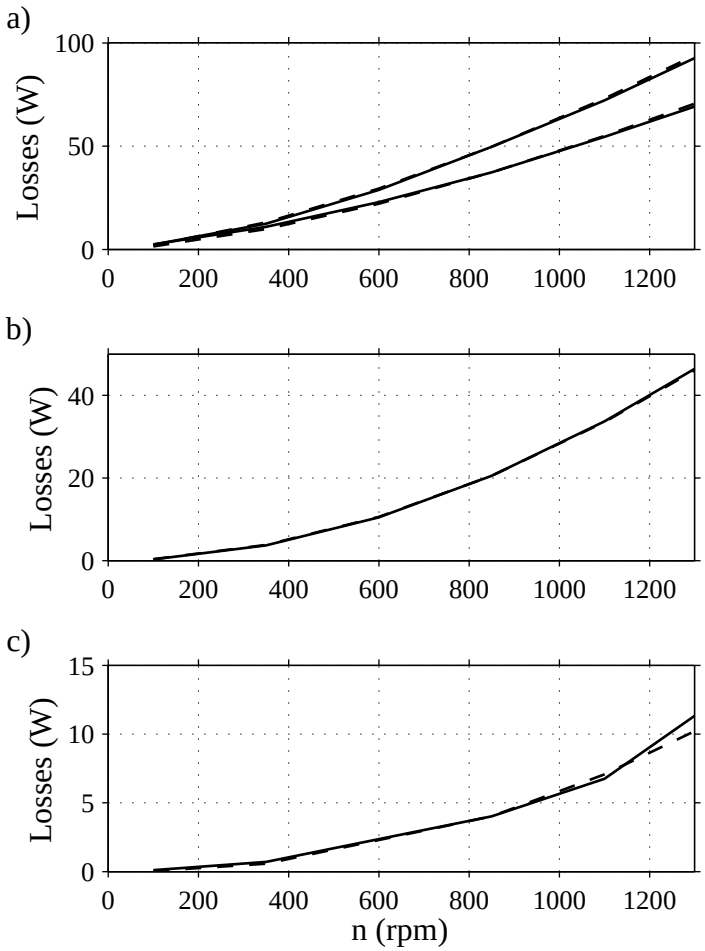

Fig. 4.4 Motor 1 FEM (solid line) and adjusted (dashed line) loss curves at rated torque for the motor parts in consideration: a) Stator yoke and teeth; b) Magnets; c) Rotor.

By inspection of Fig. 4.6, it can be seen that the motor will always work under its rated speed (850 rpm). This is reasonable if it is considered that the driving cycle corresponds to a vehicle driven in a city and that the design rated speed of the motor corresponds to approximately 70 km/h. However, the torque requirements often overpass the rated torque of the motor (170 Nm). This could represent a problem, not only because of a possible motor overloading, but also due to unreachable torque values if the required voltage exceeds the one provided by the dc-link. Both possibilities have been considered, proving that the required motor power does not exceed the rated value (15 kW) and that the required voltage never is higher than the one provided in the dc-link (350 V). Moreover, these high torque values require a current higher than the rated and thus the demagnetizing fields will become higher than the ones presented in Fig. 3.8. This implies that the maximum magnet temperature may be lower than the one calculated in Table 3.4 when running this drive cycle.

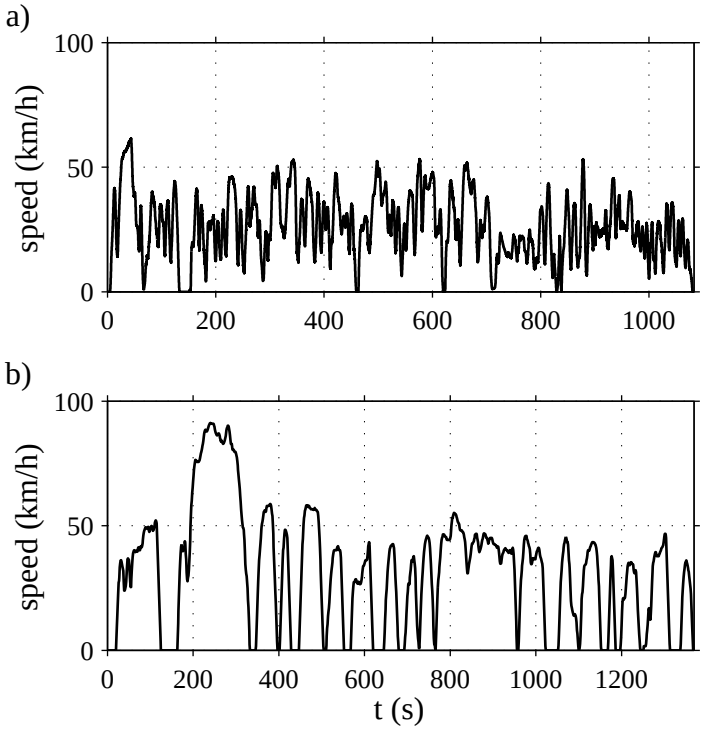

Fig. 4.5 Drive cycles: a) Urban car driving in Göteborg; b) UDDS test.

The second duty cycle, presented in Fig. 4.7, does overpass the rated speed of the motor, but never reaches the maximum design value (1872 rpm). The torque requirement is lower in this case, making always the motor function under its rated value. Again, the power output of the motor is under its nominal value.

Additionally, the motors temperatures are also evaluated at a steady state corresponding to rated torque and speed. However, in normal driving conditions, this point is not maintained for a long time since it corresponds to a very high torque and a speed of approximately 70 km/h. It could be compared with a situation in which the driver is overtaking another vehicle, or strongly accelerating to incorporate to a motor way.

4.14 Results

The results for the different motors and cases are presented in this section. As mentioned before, a coefficient of 1.5 is applied to the losses value to avoid possible underestimations and stay on the safe side. In the duty cycles, the results correspond to a steady state achieved by repeating them three times. The maximum temperature registered for each component is displayed. A cold start is considered in all cases, i.e., the initial temperature of the motor is the ambient temperature 40 ^{o}C.

Tables 4.8, 4.9 and 4.10, show the resulting maximum temperatures for different

Table 4.7: Parameters

c_d	0.3	
c_{rr}	0.012	
A_f	1.5	m^2
ρ_{air}	1.23	kg/m^3
m_v	1450	kg
m_w	60	kg
t	1.6	
R	340	mm

functioning conditions in the different parts of Motor 1, Motor 2 and Motor 3, respectively. These results do not include the axial magnet segmentation. It is evident from the data that the two driving cycles are less thermally demanding than the rated conditions.

Table 4.8: Temperatures (^{o}C) for Motor 1

Driving	City driving		UDDS test		Steady state (rated)	
Currents	Sinu.	PWM	Sinu.	PWM	Sinu.	PWM
Winding	84	84	67	67	139	142
End winding	87	88	68	68	145	148
Stator yoke	70	71	63	64	95	96
Stator teeth	79	79	66	67	124	126
Stator surface	78	79	65	66	123	125
Magnets	56	61	50	58	79	86
Rotor yoke	55	57	50	55	77	84
Rotor surface	56	58	51	58	79	86
Housing	55	57	50	53	76	81

In the following, the figures from the thermal analysis will be presented and commented. For each motor, both the city drive cycle and the UDDS test will be studied considering PWM currents for Motor 1 and Motor 2 and sinusoidal currents for Motor 3. Results with and without axial magnet segmentation will be also presented for Motor 1 and Motor 3.

Figs. 4.8 and 4.9 show the temperatures of Motor 1 fed with PWM currents driven under the city driving drive cycle and the UDDS test respectively. It can be appreciated how the windings achieve higher temperatures in the city driving test since the torque requirements are also higher. A higher torque requires higher currents and, thus, more copper losses. However, besides the UDDS test has a higher average speed, the magnet temperatures are higher in the city driving test. This is because the magnet losses are not very significant in Motor 1 and the higher winding temperatures of the city driving test heat the magnets. This can be seen from the temperature difference between the components placed in the stator and the rotor of the motor which is around 20 ^{o}C in the UDDS

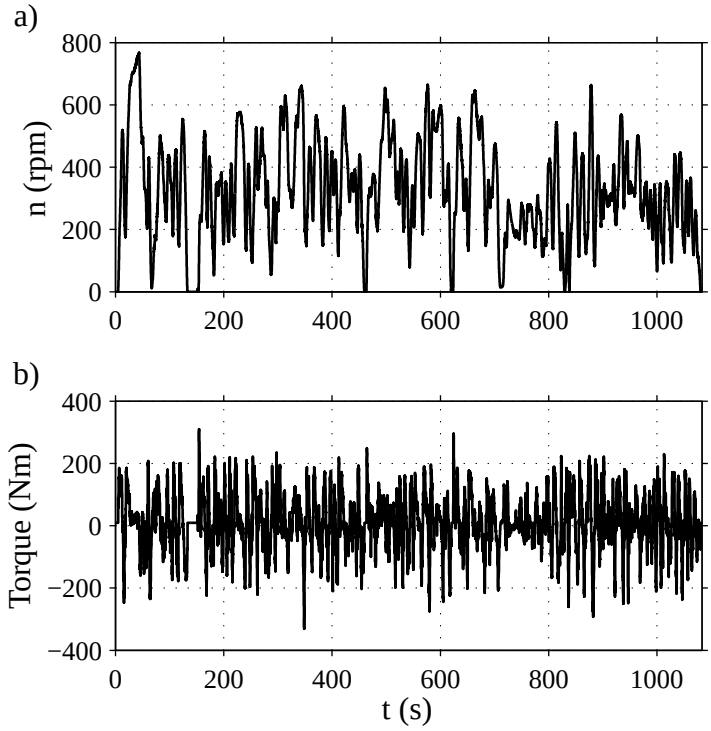

Fig. 4.6 Göteborg driving requirements: a) Motor speed; b) Motor torque.

test and 10 ^{o}C in the city driving test.

Figs. 4.11 and 4.11 show the temperatures of Motor 2 with PWM currents running under the city driving test with and without magnet segmentation respectively. Figs. 4.12 and 4.13 show the same cases but under the UDDS test. From them, it can be again appreciated how the city driving test produces higher winding temperatures than the UDDS test. When the magnet temperatures are compared, it is seen how there is a difference between both tests when the magnet losses are relatively high or low. This is, when the magnet segmentation is carried out, the city driving test produces higher magnet temperatures than the UDDS test. As it happened with Motor 1, the higher winding temperatures of the first test heat the magnets. However, when the magnet segmentation is not made, the magnet losses become sensibly higher and the higher speed of the UDDS test respect to the city driving test produces higher magnet temperatures.

Finally, the resulting temperatures in Motor 3 fed with sinusoidal currents are shown in Figs. 4.14 and 4.15 for the city driving test with and without magnet segmentation respectively and in Figs. 4.16 and 4.17 for the UDDS test in the same conditions. The high copper and magnet losses of Motor 3 increase the effect seen for the two other motors. The winding temperatures are once again higher when running the city drive test. When it comes to magnet temperatures, the low magnet losses with segmentation compared to the winding losses cause a big temperature difference between the windings and

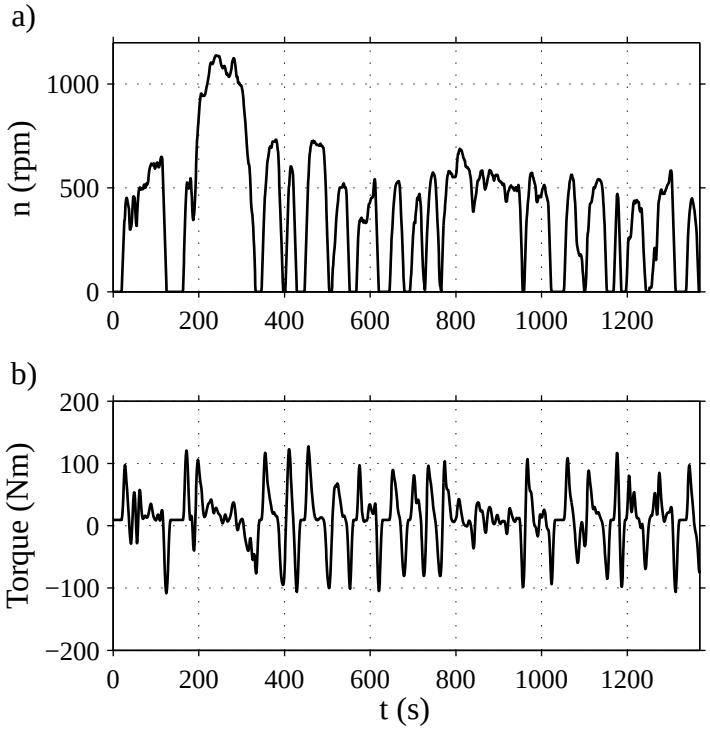

Fig. 4.7 UDDS drive cycle requirements: a) Motor speed; b) Motor torque.

the magnets in the city driving test (30 ^{o}C) with respect to the UDDS test (20 ^{o}C). Again, the magnets are heated by the windings producing a higher magnet temperature in the first test despite its lower speed requirements. However, if there is no magnet segmentation considered, the losses in this component become extremely high. The high speed of the UDDS test (especially around the second 300 of the cycle) produces that the temperatures of the magnets rise over the ones in the windings and the stator, reversing the heat exchange from stator-rotor to rotor-stator.

4.14.1 Magnet temperatures

As mentioned before in this thesis, the magnets have to be carefully observed for a possible demagnetization. Analyzing the results, it can be seen that the critical demagnetization temperatures presented in Table 3.4 are far from being reached in Motor 1 and Motor 2, neither in the driving cycles nor in the steady state at rated conditions. However, due to the high losses in the magnets of Motor 3, the demagnetization temperature (120 ^{o}C) is almost reached in the steady state (118 ^{o}C).

Although the steady state at rated conditions is not intended to be maintained for a long time, it is recommended to perform the magnet axial segmentation to reduce the magnet losses and, thus, its temperatures. Furthermore, the results obtained for Motor 3 correspond to sinusoidal currents. If PWM currents were considered, the motor losses

Table 4.9: Temperatures (°C) for Motor 2

Driving	City driving		UDDS test		Steady state (rated)	
Currents	Sinu.	PWM	Sinu.	PWM	Sinu.	PWM
Winding	73	77	64	66	111	115
End winding	78	79	65	67	119	124
Stator yoke	66	68	63	65	80	82
Stator teeth	70	72	65	68	95	99
Stator surface	70	72	64	68	94	99
Magnets	54	58	53	61	71	82
Rotor yoke	54	57	50	58	70	80
Rotor surface	54	59	53	61	71	82
Housing	54	57	50	57	69	78

Table 4.10: Temperatures (°C) for Motor 3

Driving	City driving	UDDS test	Steady state (rated)
Winding	98	72	156
End winding	101	73	164
Stator yoke	77	64	91
Stator teeth	81	67	108
Stator surface	81	67	108
Magnets	72	87	118
Rotor yoke	68	77	111
Rotor surface	72	87	118
Housing	67	72	108

would considerably increase as it happened in Motor 1 and Motor 2.

For Motor 2 fed with PWM currents, when a 6-piece axial magnet segmentation is considered, the magnet temperatures decrease from 82 °C to 70 °C in the rated case. For Motor 3 fed with sinusoidal currents, the reduction goes from 118 °C to 77 °C in the same case.

4.14.2 Winding temperatures

The winding temperatures are in this case the hot spot of the motors with the exception of Motor 3 run with the UDDS test and no axial segmentation. The critical aspect about the winding's temperature is the insulation material. At rated torque and speed the end winding temperatures are 148 °C for Motor 1, 124 °C for Motor 2 and 164 °C for Motor 3. Obviously, the temperatures under the drive cycles are lower in all cases. Since the winding insulation material was considered to be of the class H which means that it can withstand temperatures up to 180 °C and considering that the relevant temperature information should be extracted from the driving cycles and not from the rated torque and

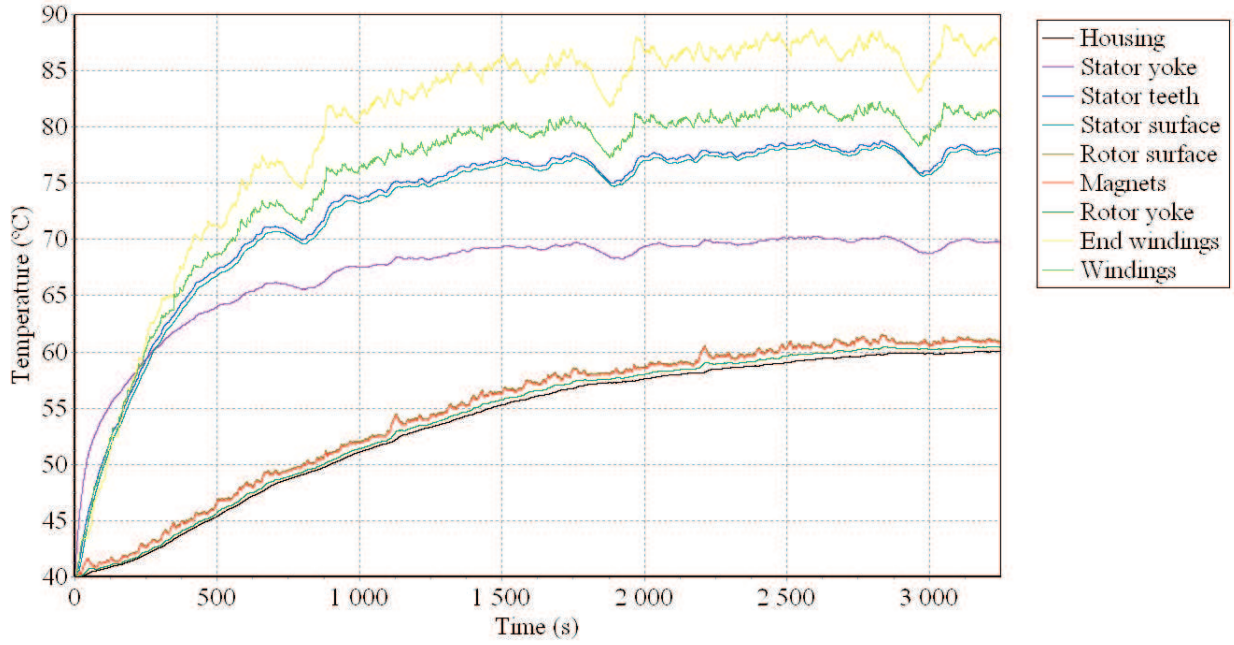

Fig. 4.8 Temperatures in Motor 1 with PWM currents and without magnet segmentation running the city driving test (three times).

speed steady state which is not intended to be maintained, it can be concluded that the current density of the motors could be increased. This would allow the motors achieve higher torques.

4.15 Parameter sensitivity

The thermal analysis results are very dependent on a good setting. Small differences in some of the key parameters will largely change the results. Thus, a parameter sensitivity analysis is made to see how the results are affected by some small changes.

This study is only made on Motor 3 with no segmentation over the steady state temperatures at rated torque and speed and its purpose is only to give an overview of the importance of some of the parameters.

4.15.1 Interface gaps

As mentioned before, the contact resistance is often more important than the actual material thermal resistance. Moreover, this parameter can suffer big differences depending on the motor construction. Fig. 4.18 shows the effect of the variation of some of the contact resistances in the model.

All three interface gaps varied have an important influence on the magnet temper-

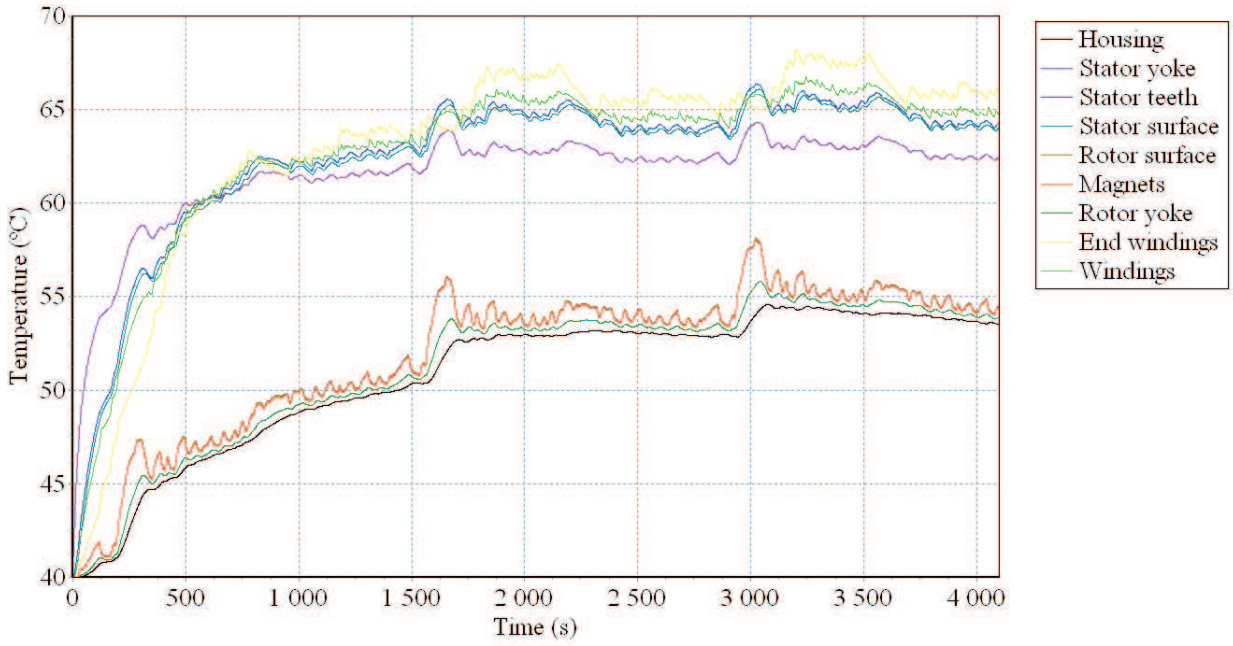

Fig. 4.9 Temperatures in Motor 1 with PWM currents and without magnet segmentation running the UDDS test (three times).

ature, especially the rotor-magnet gap. It must as accurately determined as possible from the surface conditions of the materials, since a 10 times length difference produces 15 ºC of magnet temperature variation. Moreover, if the effect of inaccurate interface gap prediction in different components is added, the temperature differences can be even higher. For the winding temperature, the interface gaps rotor-housing and rotor-magnet do not have a sensibly important effect. However, the repercussion of the spiral groove-stator interface gap variation is outstanding.

4.15.2 Cooling system

The cooling system can vary its design to fit the motor thermal requirements. Fig. 4.19 shows how the variation of the parameters that define it influences the temperature of magnets and windings. It is also useful to understand what would happen in case of a malfunction of the cooling system. A very low coolant flow implies temperatures rising over 300 ºC in the windings and 150 ºC in the magnets. It can also be seen that the cooling fluid used varies its properties with the temperature and, thus, its use is more appropriate in certain ranges. Note that the variation between the two cooling fluids used is the proportion of the mix with water and, thus, the curves behave similarly.

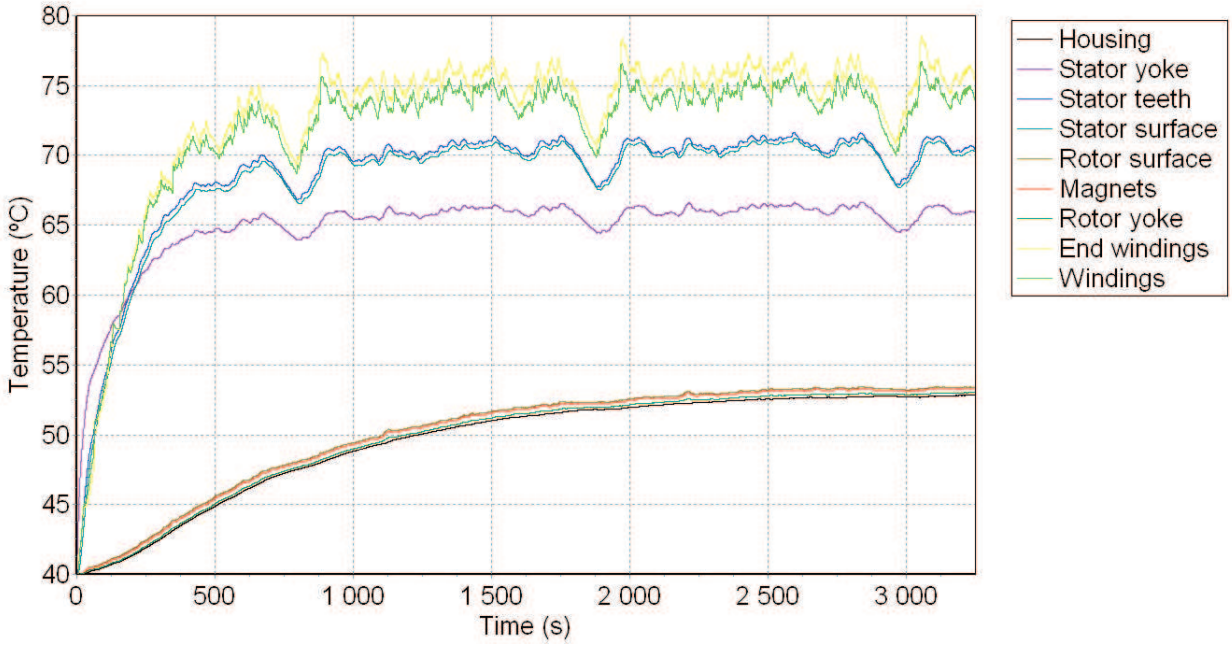

Fig. 4.10 Temperatures in Motor 2 with PWM currents and 6-piece axial magnet segmentation running the city driving test (three times).

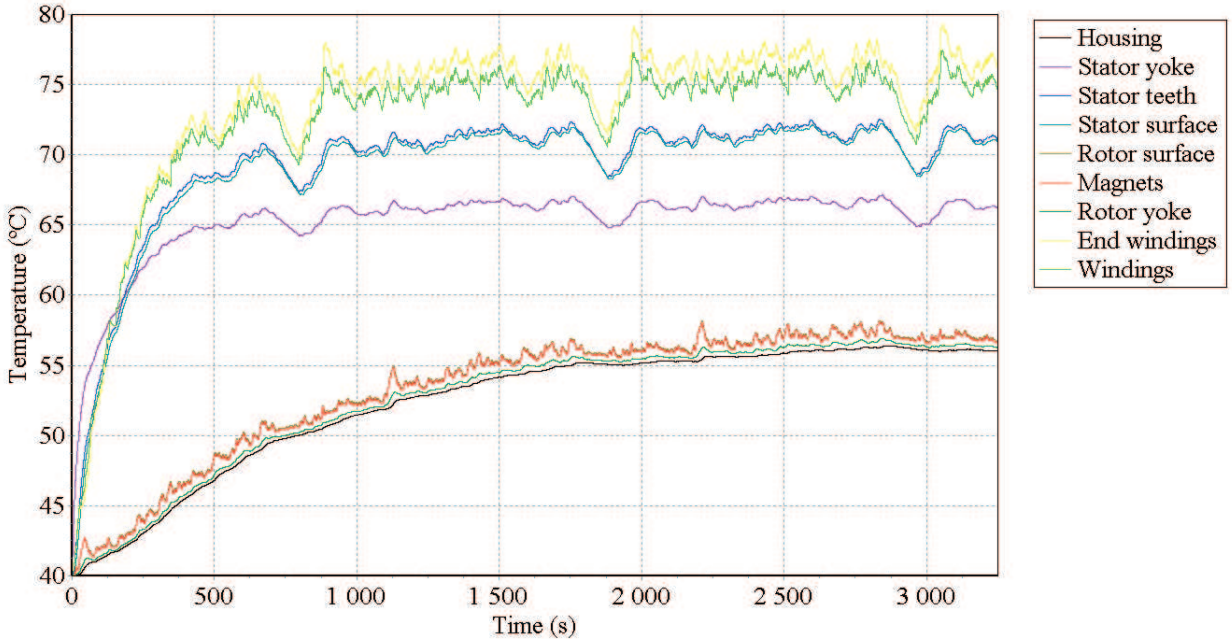

Fig. 4.11 Temperatures in Motor 2 with PWM currents and without magnet segmentation running the city driving test (three times).

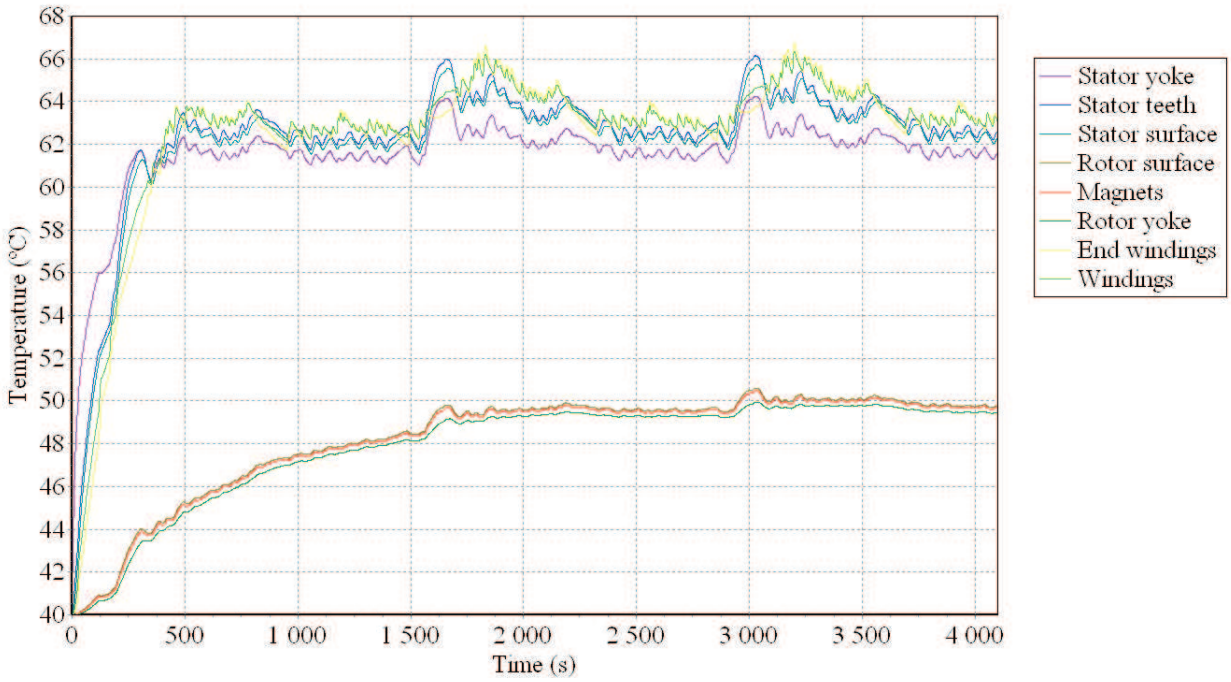

Fig. 4.12 Temperatures in Motor 2 with PWM currents and 6-piece axial magnet segmentation running the UDDS test (three times).

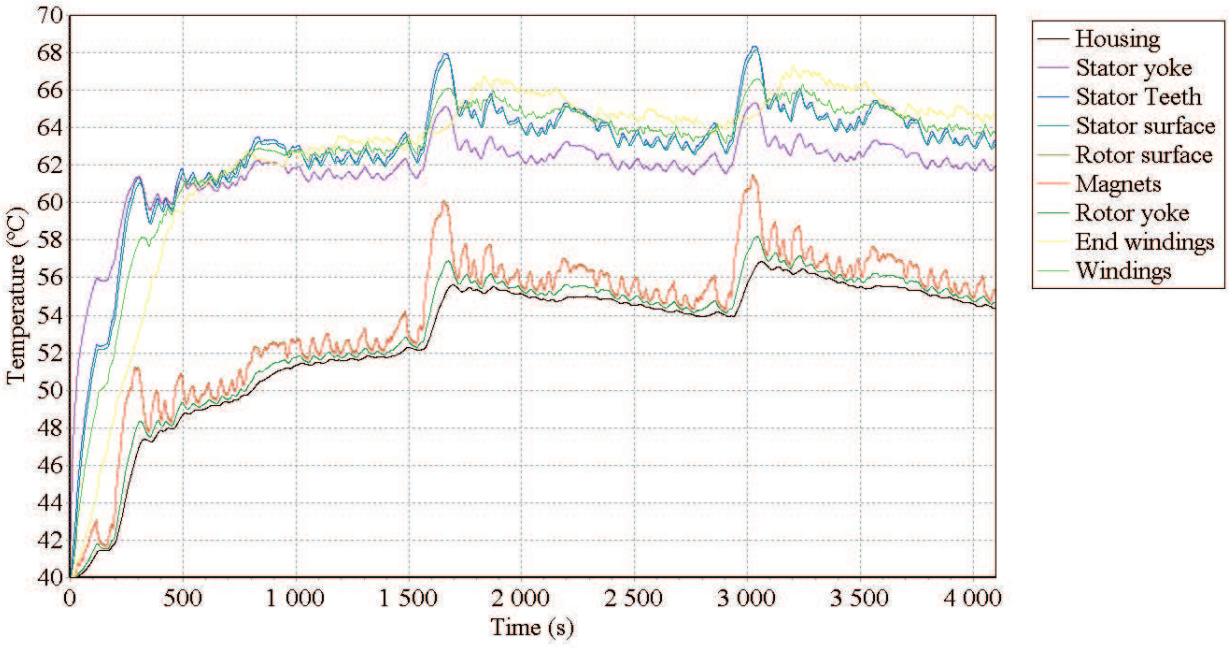

Fig. 4.13 Temperatures in Motor 2 with PWM currents and without magnet segmentation running the UDDS test (three times).

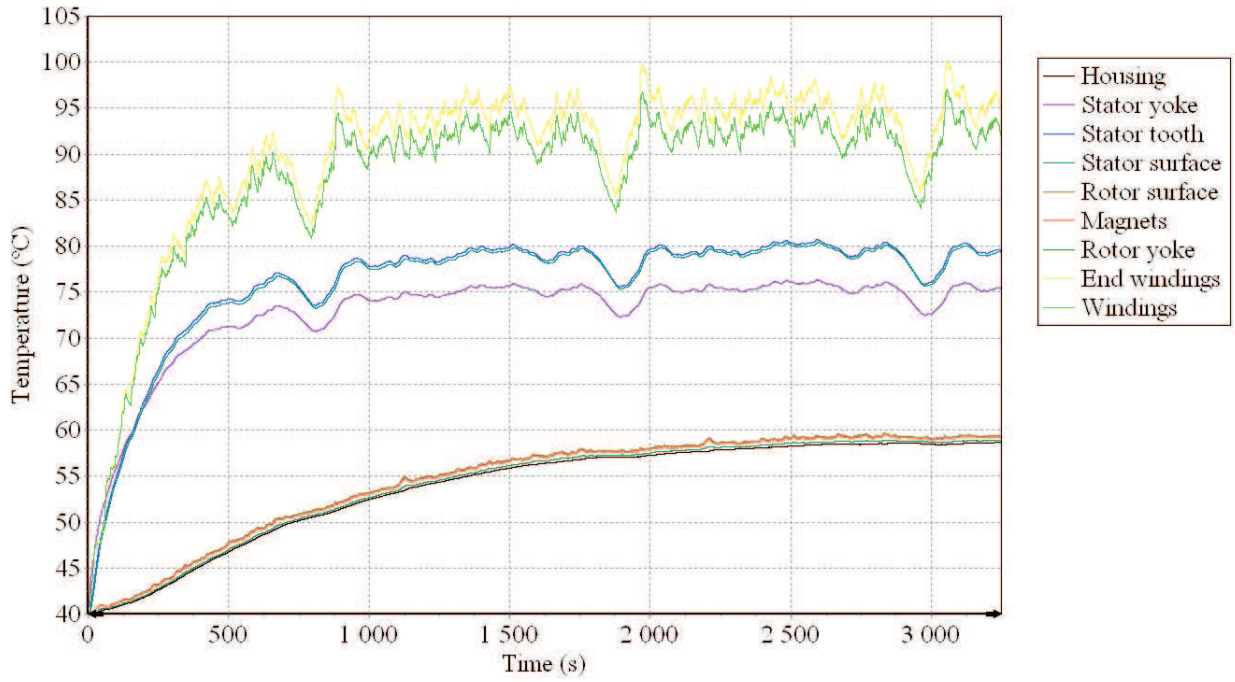

Fig. 4.14 Temperatures in Motor 3 with sinusoidal currents and 6-piece axial magnet segmentation running the city driving test (three times).

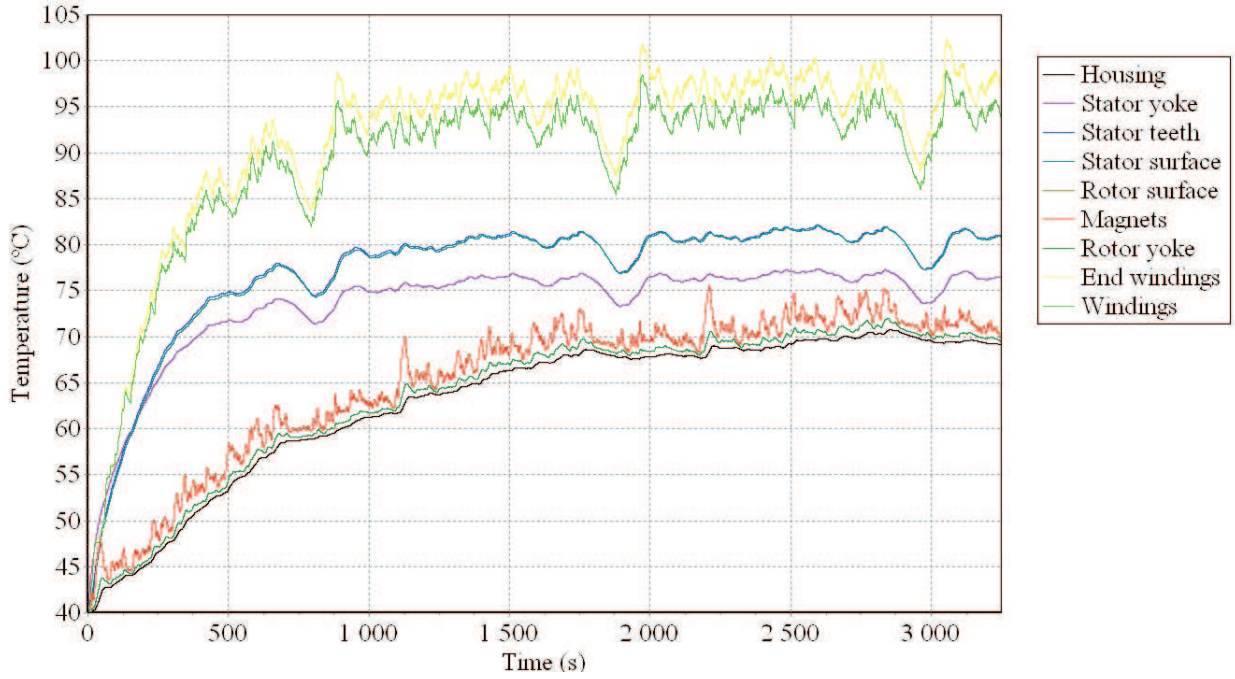

Fig. 4.15 Temperatures in Motor 3 with sinusoidal currents and without magnet segmentation running the city driving test (three times).

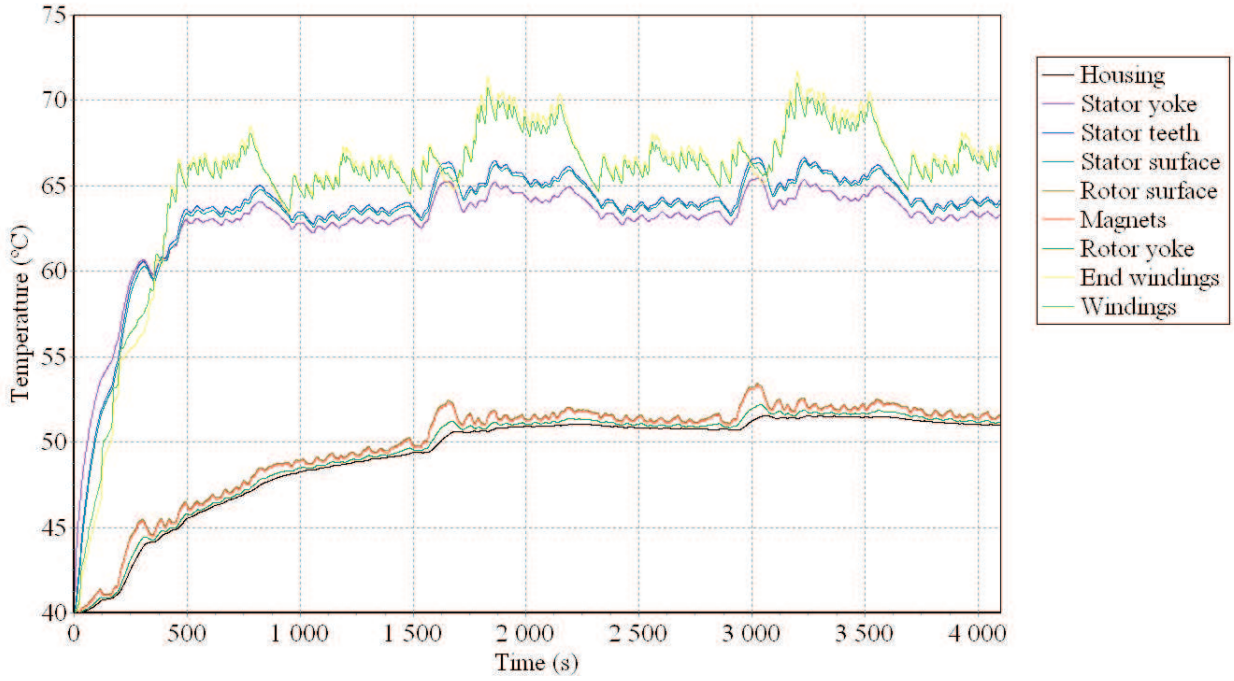

Fig. 4.16 Temperatures in Motor 3 with sinusoidal currents and 6-piece axial magnet segmentation running the UDDS test (three times).

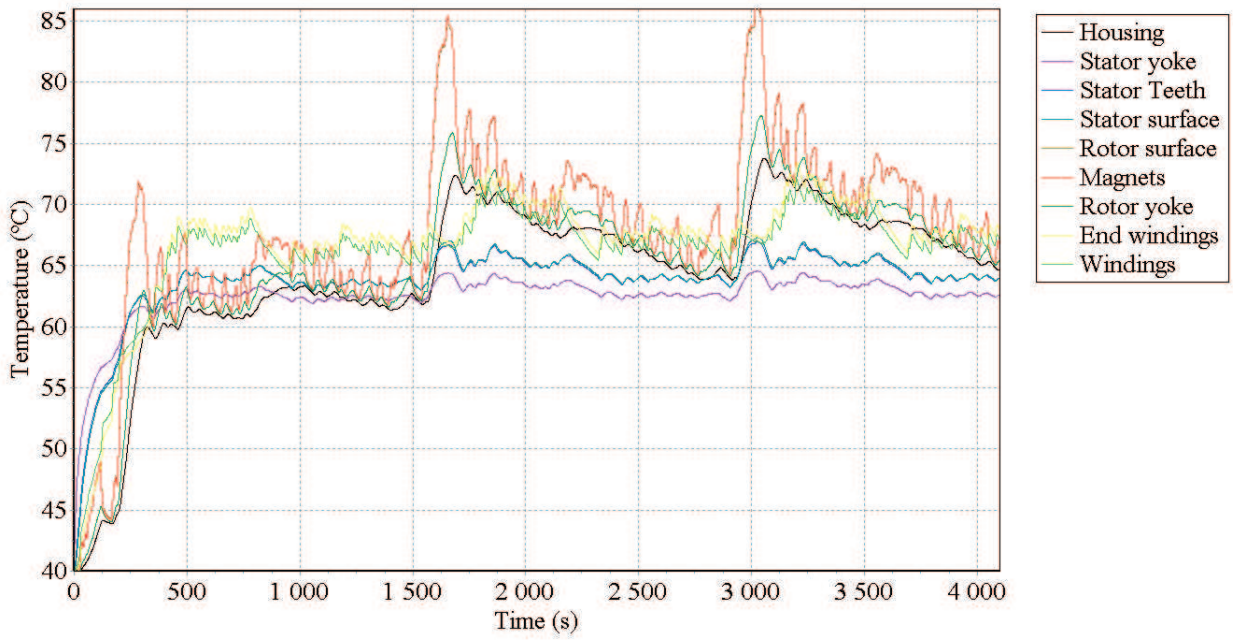

Fig. 4.17 Temperatures in Motor 3 with sinusoidal currents and without magnet segmentation running the UDDS test (three times).

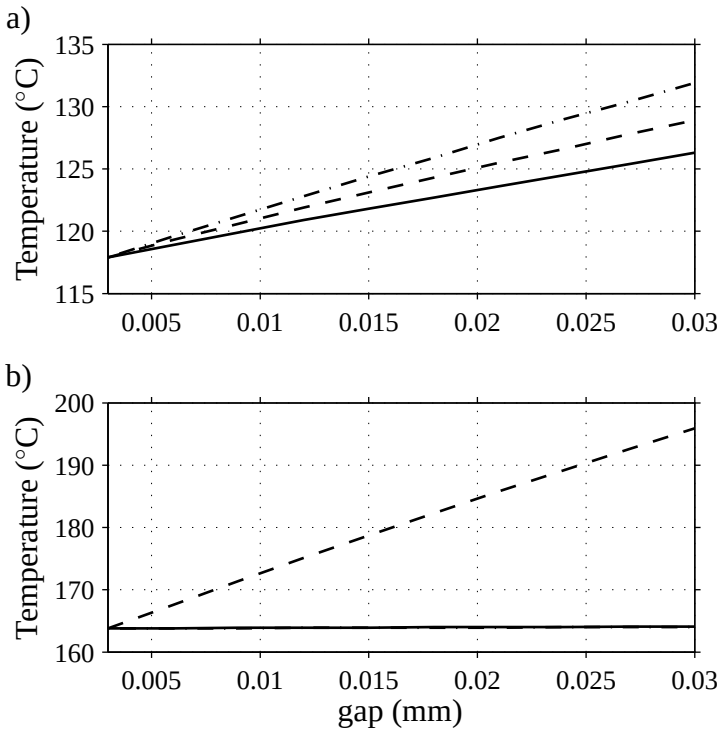

Fig. 4.18 Temperatures, varying the rotor-housing gap (solid line), the stator-spiral groove gap (dashed line) and the rotor-magnets gap (dashed-dotted line), in the sensible parts of Motor 3: a) Magnets; b) Windings.

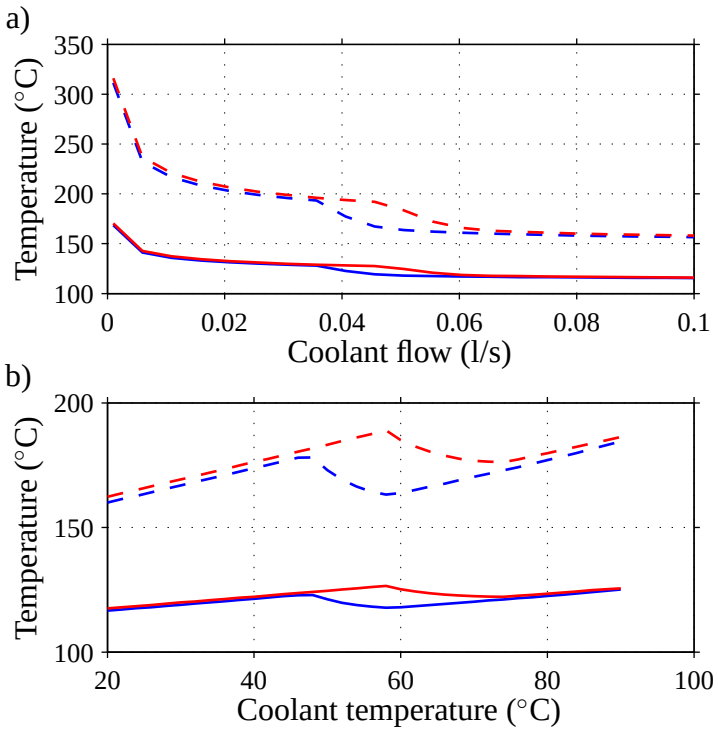

Fig. 4.19 Temperatures in the magnets (solid line) and in the windings (dashed line) with two different coolant fluids, EGW 50/50 (blue) and EGW 60/40 (red) varying the following parameters: a) Coolant flow through the spiral groove; b) Coolant inlet temperature.

Chapter 5

Conclusions and further work

This chapter summarizes conclusions and provides some suggestions for further investigations related to the topics considered in this thesis.

5.1 Conclusions

This thesis has reviewed the fundamental aspects of an analytical model of a PMSM with outer rotor. Both, distributed and concentrated winding configurations were considered and three different analytical solutions were obtained. Two of these solutions correspond to distributed winding motors (Motor 1 and Motor 2) and the third (Motor 3) is a concentrated winding motor. Light weight configurations were aimed, resulting in two light weight and high pole number solutions (Motor 2 and Motor 3) and a heavier but with lower pole number (Motor 1).

Analytical torque-speed and voltage-speed curves were obtained, resulting in a lower voltage requirement at the same speed for Motor 2 and Motor 3 than in Motor 1. Thus, the first two can achieve a higher torque at maximum speed than the latter.

A FEM analysis of the analytical configurations obtained was carried out, distinguishing between sinusoidal and PWM current input. The torque-speed and voltage-speed curves were obtained and compared to the analytical, resulting in a higher torque at high speeds than predicted in all three motors. From this comparison, the simplicity of the analytical model used can be appreciated, especially in the calculation of the inductances which leads to incorrect voltage values. Motor 3 also resulted to have a slightly lower rated torque than the one obtained by analytical means.

The torque waveforms were analyzed resulting in a much lower ripple from the concentrated winding motor. Stator skew was introduced, achieving an important ripple reduction. The high frequency ripple introduced by the PWM currents was also eliminated with this technique.

The losses in the different motor components were computed, both with sinusoidal and PWM currents. Motor 1 resulted to have the lowest iron and magnet losses, but the

lowest copper losses were obtained in Motor 2. The concentrated winding solution (Motor 3) had substantially higher magnet losses than the distributed winding configurations. An analytical magnet segmentation model was applied to Motor 2 and Motor 3, resulting in an important decrease of the magnet losses in both cases.

Further, a thermal analysis of the motors was conducted. The temperatures of the motors were obtained under two different drive cycles and at the steady state in rated conditions. They were contrasted with the material properties of the magnets to evaluate the viability of the motors, i.e., avoid their irreversible demagnetization. Motor 1 and Motor 2 appeared to have no thermal problems, but Motor 3 was close to the magnet limits in the rated torque and speed steady state when the magnet segmentation was not considered. Winding temperatures were contrasted with the winding insulation material properties and it was concluded that a higher current density could be achieved.

Finally, a sensibility analysis of the thermal analysis was carried out were the importance of some of the parameters such as the interface gaps was highlighted.

5.2 Recommendations for further work

It has been seen how the analytical results differ from the ones obtained in the FEM analysis. Thus, since the optimization process is made on an analytical basis, it is recommended to use a more advanced analytical model to find a possible lighter configuration. There might be lighter motor configurations which have been discarded based on erroneous voltage values.

The FEM analysis completed in this thesis is two dimensional only. Due to the short axial length of the motors in consideration, there is a considerable axial end effect that is neglected in this case. Thus, a 3D analysis is recommended to account for that effect and confirm the results. Moreover, with a 3D analysis the stator skew and magnet segmentation could also be implemented and its effect calculated with accuracy.

Furthermore, the motor design process requires a feedback loop. Thus, with the results obtained in this thesis, the loop should be closed changing those parts of the design susceptible of improvement, e.g. tooth shapes could be designed to obtain a smoother flux distribution and reduce the steel losses.

To achieve a more reliable thermal analysis, a motor model could be built to determine more accurately parameters that have a crucial importance in the heat transfer such as the interface gaps or others that have been approximated and that are very difficult to predict without building a motor prototype like the end windings.

Appendix A

Analytical motor data

		Motor 1	Motor 2	Motor 3
Motor requirements				
Rated torque	Nm	170	170	170
Rated speed	rpm	850	850	850
Max. speed	rpm	1872	1872	1872
Torque at maximum speed	Nm	59	69	90
Max. fund. phase current (rms)	A	42	53	54
Max. fund. current density (rms)	A/mm^2	10	10	10
Current loading (rms)	kA/m	34.7	32.6	32.8
Min. dc-link voltage	V	339	251	251
Geometrical spec.				
Physical air gap length	mm	1	1	1
Inner radius	mm	158.5	173.0	179.6
Outer radius	mm	216	216	216
Stator outer radius	mm	196.3	202.2	203.4
Total slot width	mm	5.9	7.4	19.9
Total slot depth	mm	21.8	19.7	15
Tooth width	mm	6.9	8.8	22.7
Slot insulation thickness	mm	0.2	0.2	0.2
Thickness of stator back	mm	16	9.6	8.8
Thickness of rotor back	mm	16	10	9
Active length	mm	30	30	30
Magnet thickness	mm	2.7	2.8	2.6
Active weight	kg	17.0	12.2	12.6
Magnet weight	kg	0.5	0.5	0.5

Appendix A. Analytical motor data

Electrical data				
Phase resistance	mΩ	206	90	136
Permanent magnet flux linkage	Vs	0.24	0.12	0.11
$d-$axis air gap inductance	mH	1.71	0.38	0.34
$q-$axis air gap inductance	mH	1.71	0.38	0.34
Slot leakage inductance	mH	0.23	0.11	0.10
$d-$axis current at rated operation	A	0	0	0
$q-$axis current at rated operation	A	59.4	75.0	77.0
Loss data				
Copper losses at rated operation	kW	1.09	0.76	1.21
Iron losses at rated operation	kW	0.07	0.09	0.07
Efficiency at rated operation	-	0.93	0.95	0.92
Winding spec.				
Connection type	-	series connected Y		
Number of poles	-	16	26	28
Number of slots per pole and phase	-	2	1	0.357
Number of turns per slot	-	11	10	27
Fundamental winding factor	-	0.966	1	0.951
Copper fill factor	-	0.45	0.45	0.60
Flux density data				
Air gap peak fund. density	-	1.04	0.99	0.97
Peak fund. flux density in stator back	T	1.6	1.6	1.6
Peak fund. flux density in stator teeth	T	1.6	1.6	1.6
Peak fund. flux density in rotor back	T	1.60	1.54	1.57
Magnet data				
Remanent flux density at operating temp.	T	1.2	1.2	1.2
Relative permeability	-	1.05	1.05	1.05
Magnet density	kg/m^3	7700	7700	7700
Steel data				
Eddy current loss density constant	Ws^2/kgT^{2}rad^2	$1.19{\cdot}10^{-6}$	$1.19{\cdot}10^{-6}$	$1.19{\cdot}10^{-6}$
Steinmetz constant	-	2	2	2
Hysteresis loss density constant	Ws/kgT$^\beta$rad	$3.1{\cdot}10^{-3}$	$3.1{\cdot}10^{-3}$	$3.1{\cdot}10^{-3}$
Steel density	kg/m	7700	7700	7700
Other spec.				
Copper resistivity at operating temp.	nΩm	23.9	23.9	23.9
Copper density	kg/m^3	8930	8930	8930

Appendix A. Analytical motor data

Appendix B

Basic vehicle dynamics

The basic dynamics of a vehicle are described in (B.1) by simply applying Newton's second law which results in

$$(m_v + m_w)\, a = F_d - F_{rr} - F_w \tag{B.1}$$

where a is the vehicle's linear acceleration, F_d is the driving force, F_{rr} is the rolling resistance, F_w is the wind resistance and m_v and m_w are the vehicle and wheels mass respectively. The rolling resistance force for the whole vehicle is given by

$$F_{rr} = c_{rr}\,(m_v + m_w)\, g \tag{B.2}$$

where c_{rr} is the rolling resistance coefficient and g is the gravity acceleration. The wind resistance can be expressed as

$$F_w = \frac{1}{2} c_d A_f \rho_{\text{air}} v^2 \tag{B.3}$$

where c_d is the drag coefficient, A_f is the vehicle's front area, ρ_{air} is the density of the air and v is the speed of the vehicle.

Considering that all four wheels are driven with equal motors, it is assumed that the torque is equally distributed between the front and back wheels and that a gearbox of ratio t is equipped on each wheel of radius R, the torque required for each motor can be expressed as

$$T_m = \frac{1}{t}\frac{R}{4}\left[(m_v + m_w)\, a + \frac{1}{2} c_d A_f \rho_{\text{air}} v^2 + c_{rr}\,(m_v + m_w)\, g\right]. \tag{B.4}$$

Appendix C

Basic heat transfer numbers

The dimensionless groups of heat and mass transfer used for the correlations in the thermal analysis described in Chapter 4 are [6]:

- **Reynolds** number: Ratio of inertia and viscous forces.

$$Re = \frac{vL}{\nu} \tag{C.1}$$

  where v is the speed of the fluid (m/s), ν its kinematic viscosity (m^2/s) and L the characteristic length (m).

- **Prandtl** number: Ratio of momentum and thermal diffusivities.

$$Pr = \frac{c_p \mu}{\kappa} \tag{C.2}$$

  where c_p is the specific heat at constant pressure (J/(kgK)) of the material, κ the thermal conductivity (W/(mK)) and μ is the viscosity (kg/s).

- **Nusselt** number: Dimensionless temperature gradient at the surface.

$$Nu = \frac{hL}{\kappa} \tag{C.3}$$

  where h is the convection heat transfer coefficient ($W/(m^2K)$), κ the thermal conductivity (W/(mK)) and L the characteristic length (m).

- **Grashof** number: Ratio of buoyancy to viscous forces.

$$Gr = \frac{g\beta\left(T_s - T_\infty\right)L^3}{\nu^2} \tag{C.4}$$

  where g is the gravity acceleration (m/s^2), β is the volumetric thermal expansion coefficient (1/K), T_s and T_∞ the surface temperature and ambient temperature respectively (K), ν the kinematic viscosity (m^2/s) and L the characteristic length (m).

Appendix D

List of symbols, subscripts and abbreviations

Symbols

a	acceleration
b_{so}	slot opening width
b_{ss1}	slot top width
b_{ss2}	slot base width
b_{st}	tooth width
c_d	drag coefficient
c_f	Carter factor
c_p	specific heat at constant pressure
c_{rr}	rolling resistance coefficient
f	input frequency
f_{cog}	cogging frequency
f_d	function
f_q	function
f_{w1}	fundamental winding factor
ff	copper fill factor
g	gravity acceleration
h	convection heat transfer coefficient
h_m	magnet height
h_r	radiation heat transfer coefficient
h_{ry}	rotor yoke height
h_{ss}	stator slot height
h_{sw}	stator tooth tip height
h_{sy}	height of the stator yoke
i	peak fundamental phase current, integer
k	constant, integer

l	magnet segment axial length, characteristic length
m_{st}	weight of the stator teeth
m_{sy}	weight of the stator yoke
m_v	vehicle weight
m_w	wheel weight
n	mechanical rotor speed
n_r	rated mechanical rotor speed
n_s	number of turns per slot
n_{sl}	stator skew in number of slots
p	number of poles
q	number of slots per pole and phase
r_{in}	motor inner radius
r_{out}	motor outer radius
r_δ	air gap radius
t	time, gearbox ratio
u	peak fundamental voltage
v	velocity
w	magnet segment width
y_{sp}	pitch length in number of slots
A_f	vehicle front area
B	magnetic flux density
B_r	remanent magnetic flux density
B_{sy}	magnetic flux density in the stator yoke
B_δ	peak fundamental air gap flux density
D	inner stator diameter
E	peak fundamental phase voltage
F	view factor
F_d	driving force
F_{rr}	rolling resistance force
F_w	wind resistance force
Gr	Grashof number
H	magnetic field intensity
H_c	coercive field strength
${}_iH_c$	intrinsic coercivity
J	peak fundamental current density
L	motor active length
L_{leak}	leakage inductance
L_s	synchronous inductance
Nu	Nusselt number
N_z	number of axial magnet segments per pole

P	power loss
Pr	Prandtl number
Q	number of slots
R	wheel radius
Re	Reynolds number
R_s	stator resistance
S_1	peak fundamental current loading
T	temperature
T_e	electro-mechanical torque
T_r	rated torque
T_∞	ambient temperature
α	mechanical angle covered by one magnet, coefficient
α_{elec}	electrical angle covered by one magnet
β	Steinmetz constant,
δ	air gap length
δ_{skin}	electrical skin depth
ε	surface emissivity
θ	mechanical angle
θ_e	electrical rotor angle (position)
θ_s	mechanical skew angle
κ	thermal conductivity
μ	magnetic permeability
μ_0	magnetic permeability of vacuum
μ_r	relative magnetic permeability
ν	kinematic viscosity
ρ	electrical resistivity, density
ρ_{Cu}	copper density
ρ_m	magnet density
ρ_s	steel density
σ	Stephan-Boltzmann constant
ϕ	angular phase shift
ψ	flux linkage
ψ_m	permanent magnet flux linkage
ω	electrical rotor speed, angular frequency of the current

Subscripts

a	phase a component
b	phase b component
c	phase c component
d	direct-axis component

forc.	forced convection
hyst	hysteresis
max	maximum
mean	mean value
min	minimum
mix	mixed convection
nat.	naturalconevction
q	quadrature-axis component
r	rated value
ref	reference value
sat	saturation
surf	surface
turb.	turbulent flow
vort.	vortex flow
0	without segmentation

Abbreviations

dc	direct current
fund.	fundamental
max	maximum
min	minimum
overlap.	overlapping
ref	reference
rms	root mean square
sat	saturation
sinu.	sinusoidal
spec.	specification
ACM	autonomous corner module
CW	concentrated windings
DW	distributed windings
Eq	equation
FEM	finite element method
FFT	fast Fourier transformation
Fig.	figure
MMF	magnetomotive force
PM	permanent magnet
PMSM	permanent magnet synchronous machine
PWM	pulse width modulation
2D	2 dimensional
3D	3 dimensional

Appendix D. List of symbols, subscripts and abbreviations

References

[1] W. Adams, U.S. Patent 300 827, 1884.

[2] C. Gazley, "Heat transfer characteristics of rotating and axial flow between concentric cylinders," *Trans ASME*, Jan. 1958.

[3] J. F. Gieras and M. Wing, *Permanent magnet motor technology*. New York, USA: Marcel Dekker, Inc., 2002.

[4] D. Hanselman, *Brushless Permanent Magnet Motor Design*. Orono, USA: The Writers' Collective, 2003.

[5] W.-Y. Huang, A. Bettayeb, R. Kaczmarek, and J.-C. Vannier, "Optimization of magnet segmentation for reduction of eddy-current losses in permanent magnet synchronous machine." *Energy Conversion, IEEE Transactions on*, June 2010.

[6] F. P. Incropera, D. P. D. Witt, T. L. Bergman, and A. S. Lavine, *Fundamentals of Heat and Mass Transfer*. New York, USA: Wiley, cop, 2007.

[7] T. Jahns and W. Soong, "Pulsating torque minimization techniques for permanent magnet ac motor drives-a review." *Industrial Electronics, IEEE Transactions on*, Apr. 1996.

[8] M. Jonasson, "Exploiting individual wheel actuators to enhance vehicle dynamics and safety in electric vehicles." Doctoral Thesis, Royal Inst. Technol., Stockholm, Sweden, 2009.

[9] H. Jussila, P. Salminen, M. Niemela, and J. Pyrhonen, "Guidelines for designing concentrated winding fractional slot permanent magnet machines," *POWERENG2007 International Conference on Power Engineering - Energy and Electrical Drives Proceedings*, pp. 191–194, Apr. 2007.

[10] F. Libert, "Design, optimization and comparison of permanent magnet motor for a low-speed direct-driven mixer," Licentiate Thesis, Royal Inst. Technol., Stockholm, Sweden, 2004.

[11] F. Libert and J. Soulard, "Investigation on pole-slot combinations for permanent-magnet machines with concentrated windings," *16th International Conference on Electrical Machines. Conference Proceedings*, Sept. 2004.

[12] F. Magnussen and C. Sadarangani, "Winding factors and joule losses of permanent magnet machines with concentrated windings," *Electric Machines and Drives Conference, 2003. IEMDC'03. IEEE International*, June 2003.

[13] F. Meier, "Permanent-magnet synchronous machines with non-overlapping concentrated windings for low-speed direct-drive applications," Doctoral Thesis, Royal Inst. Technol., Stockholm, Sweden, 2008.

[14] A. F. Mills, *Basic Heat and Mass Transfer*. Upper Saddler River, N.J.: Prentice Hall, 1999.

[15] C. Sadarangani, *Electrical Machines. Design and Analysis of Induction and Permanent Magnet Motors*. Stockholm, Sweden: Royal Inst. Technol., 2006.

[16] J. Simonson, *Engineering Heat Transfer*. Basingstoke, UK: MacMillan, 1998.

[17] D. Staton, A. Boglietti, and A. Cavagnino, "Solving the more difficult aspects of electric motor thermal analysis in small and medium size industrial induction motors," *Electric Machines and Drives Conference, 2003. IEMDC'03. IEEE International*, June 2003.

[18] G. Taylor, "Distribution of velocity and temperature between concentric cylinders," *Proc Roy Soc*, 1935.

[19] (2010) Vacuumschmeltze brochure. [Online]. Available: http://www.vacuumschmelze.de/index.php?id=242&L=2

[20] K. Yamazaki and K. Kitayuguchi, "Teeth shape optimization of surface and interior permanent-magnet motors with concentrated windings to reduce magnet eddy current losses," *Electrical Machines and Systems (ICEMS), 2010 International Conference.*, Oct. 2010.

[21] S. Zetterström, Sweden Patent EP1 144 212, 1994.